JCI insight

# Constitutive deletion of the obscurin-Ig58/59 domains induces atrial remodeling and Ca2+-based arrhythmogenesis

Alyssa Grogan, … , Maura Greiser, Aikaterini Kontrogianni-Konstantopoulos

*JCI Insight.* 2025. https://doi.org/10.1172/jci.insight.184202.

Research In-Press Preview Muscle biology

Obscurin is a giant protein that coordinates diverse aspects of striated muscle physiology. Obscurin immunoglobulin domains 58/59 (Ig58/59) associate with essential sarcomeric and $Ca^{2+}$ cycling proteins. To explore the pathophysiological significance of Ig58/59, we generated the *Obscn-ΔIg58/59* mouse model, expressing obscurin constitutively lacking Ig58/59. Males in this line develop atrial fibrillation by 6-months, with atrial and ventricular dilation by 12-months. As *Obscn-ΔIg58/59* left ventricles at 6-months exhibit no deficits in sarcomeric ultrastructure or $Ca^{2+}$ signaling, we hypothesized that susceptibility to arrhythmia may emanate from the atria. Ultrastructural evaluation of male *Obscn-ΔIg58/59* atria uncovered prominent Z-disk streaming by 6-months and further misalignment by 12-months. Relatedly, isolated *Obscn-ΔIg58/59* atrial cardiomyocytes exhibited increased $Ca^{2+}$ spark frequency and age-specific alterations in Ca2+ cycling dynamics, coinciding with arrythmia onset and progression. Quantitative analysis of the transverse-axial tubule (TAT) network using super-resolution microscopy demonstrated significant TAT depletion in *Obscn-ΔIg58/59* atria. These structural and $Ca^{2+}$ signaling deficits were accompanied by age-specific alterations in the expression and/or phosphorylation of T-cap, which links transverse-tubules to Z-disks, and junctophilin-2, which connects transverse-tubules to the sarcoplasmic reticulum. Collectively, our work establishes the *Obscn-ΔIg58/59* model as a reputable genetic model for atrial cardiomyopathy and provides mechanistic insights into atrial fibrillation and remodeling.



# Constitutive deletion of the obscurin-Ig58/59 domains induces atrial remodeling and $Ca^{2+}$-based arrhythmogenesis

Alyssa Grogan[1*], Annie Brong[1*], Humberto C. Joca[2], Liron Boyman[3,4,5], Aaron D. Kaplan[3,6], Christopher W. Ward[2], Maura Greiser[3,7], and Aikaterini Kontrogianni-Konstantopoulos[1,4,#]

[1]Department of Biochemistry and Molecular Biology, University of Maryland School of Medicine, Baltimore, MD 21201

[2]Department of Orthopedics, University of Maryland School of Medicine, Baltimore, MD 21201

[3]Department of Physiology, Center for Biomedical Engineering and Technology, University of Maryland School of Medicine, Baltimore, MD 21201

[4]Marlene and Stewart Greenebaum NCI Comprehensive Cancer Center, University of Maryland School of Medicine, Baltimore, Maryland, USA.

[5]Current address: Department of Physiology, Anatomy and Genetics, University of Oxford, Oxford OX1 3PT, UK.

[6]Department of Medicine and Division of Cardiology, University of Maryland Baltimore, School of Medicine, Baltimore, Maryland, USA

[7]Claude D. Pepper Older Americans Independence Center, University of Maryland School of Medicine, Baltimore, Maryland, USA.

*: Equally contributing authors

# Correspondence to: Aikaterini Kontrogianni-Konstantopoulos, PhD
Phone: 410-706-5788
Fax: 410-706-8297
e-mail: akontrogianni@som.umaryland.edu

**Author Contributions:** Conceptualization (1), data curation (2), formal analysis (3), funding acquisition (4), investigation (5), methodology (6), project administration (7), resources (8), software (9), supervision (10), validation (11), visualization (12), writing original draft (13), writing, review and editing (14).

AG: 1, 2, 3, 5, 6, 11, 12, 13, 14
AB: 1, 2, 3, 5, 6, 11, 12, 13, 14
HCJ: 3, 5, 6, 9, 10, 11, 12, 14
LB: 3, 5, 6, 9, 11, 14
ADK: 3, 5, 6, 9, 11, 14
CWW: 7, 8, 10, 14
MG: 2, 3, 5, 6, 7, 8, 10, 11, 12, 14
AKK: 1, 4, 7, 8, 10, 14

**Conflict of interest statement:** The authors have declared no conflict of interest exists.

**Keywords:** obscurin, atrial cardiomyopathy, atrial fibrillation, $Ca^{2+}$ cycling and sparks, T-cap, Z-disk

**Abstract**

Obscurin is a giant protein that coordinates diverse aspects of striated muscle physiology. Obscurin immunoglobulin domains 58/59 (Ig58/59) associate with essential sarcomeric and $Ca^{2+}$ cycling proteins. To explore the pathophysiological significance of Ig58/59, we generated the *Obscn-ΔIg58/59* mouse model, expressing obscurin constitutively lacking Ig58/59. Males in this line develop atrial fibrillation by 6-months, with atrial and ventricular dilation by 12-months. As *Obscn-ΔIg58/59* left ventricles at 6-months exhibit no deficits in sarcomeric ultrastructure or $Ca^{2+}$ signaling, we hypothesized that susceptibility to arrhythmia may emanate from the atria. Ultrastructural evaluation of male *Obscn-ΔIg58/59* atria uncovered prominent Z-disk streaming by 6-months and further misalignment by 12-months. Relatedly, isolated *Obscn-ΔIg58/59* atrial cardiomyocytes exhibited increased $Ca^{2+}$ spark frequency and age-specific alterations in $Ca^{2+}$ cycling dynamics, coinciding with arrythmia onset and progression. Quantitative analysis of the transverse-axial tubule (TAT) network using super-resolution microscopy demonstrated significant TAT depletion in *Obscn-ΔIg58/59* atria. These structural and $Ca^{2+}$ signaling deficits were accompanied by age-specific alterations in the expression and/or phosphorylation of T-cap, which links transverse-tubules to Z-disks, and junctophilin-2, which connects transverse-tubules to the sarcoplasmic reticulum. Collectively, our work establishes the *Obscn-ΔIg58/59* model as a reputable genetic model for atrial cardiomyopathy and provides mechanistic insights into atrial fibrillation and remodeling.

## Introduction

Atrial cardiomyopathy (ACM) is a complex disease that unifies etiologically distinct dysfunction initiated in the upper chambers of the heart. It was codified into histopathological classes in 2016 by the European Heart Rhythm Association (EHRAS), characterized by contractile, interstitial, and electrophysiological alterations and divided into four non-hierarchical classes (1). While ACM is a highly heterogeneous condition with respect to phenotypes and causative forces, atrial fibrillation (AF) and dilation are hallmarks of the disease shared across all four classes of ACM (1). AF is the most common arrhythmia worldwide and is associated with high morbidity and mortality (2). Changes in atrial conduction, shortening of the atrial action potential, and ectopic focal activity contribute to AF (3, 4). Importantly, a positive feedback loop exists where the structural and electrical remodeling which begets AF is perpetuated by prolonged AF, intrinsically escalating ACM (1, 3).

Given the recent recognition of ACM as a widespread clinical entity, basic science is unequipped with analogous model systems. Several animal models of AF involve exogenous intervention, such as electrode implantation for rapid atrial pacing, vagal interference, or surgery that abruptly initiate episodes of fibrillation (5, 6). These models often fail to mimic the progressive nature of AF, which gradually advances from a paroxysmal to persistent presentation. Furthermore, some surgical models and many genetic mouse models that feature AF have a preeminent ventricular cardiomyopathy or heart failure, such that atrial disturbances may be ancillary (3). Accordingly, there are few, primarily large, animal models where structural and electrical remodeling of the atria is clearly antecedent to or independent of ventricular dysfunction

(7). Here, we present a mouse model that phenocopies key features of human AF, generated by the deletion of two domains within the *OBSCN* gene.

Obscurin (720-870 kDa), encoded by the *OBSCN* gene, is a giant protein harboring both cytoskeletal and signaling modalities that encircles myofibrils along M-bands and Z-disks. Obscurin serves essential roles in myofibrillar assembly, cell adhesion, $Ca^{2+}$ signaling, and the integration of the sarcomere with the surrounding membrane and cytoskeletal structures (8, 9). Rare and deleterious variants in *OBSCN* have been increasingly associated with the development of cardiomyopathy in humans, as >20 missense, splicing, and frameshift mutations have been identified in patients with hypertrophic (HCM) and dilated (DCM) cardiomyopathy, left ventricular non-compaction (LVNC), and arrhythmogenic right ventricular cardiomyopathy (ARVC) (10-12). While the pathophysiological consequences of most known *OBSCN* mutations remain unresolved, our lab previously generated the *Obscn-R4344Q* mouse model containing the HCM-linked point mutation, R4344Q, residing within immunoglobulin (Ig) domain 58 (13). Sedentary *Obscn-R4344Q* mice developed spontaneous ventricular arrhythmia by 12-months associated with increased $Ca^{2+}$ cycling kinetics, linked to enhanced binding of phospholamban (PLN) to mutant Ig58-R4344Q (13).

The obscurin-Ig58/59 module interacts with indispensable regulators of muscle structure and function, including PLN, the Z-disk localized $NH_2$-terminal region of titin (3-4 MDa), and the titin splice variant novex-3 (~700 kDa) (13-15). Consequently, we generated the *Obscn-ΔIg58/59* mouse model that expresses endogenous obscurin constitutively lacking Ig58/59 (16). Our initial characterization revealed that sedentary *Obscn-ΔIg58/59* male animals develop spontaneous AF

by 6-months that is greatly exacerbated by 12-months, when atrial enlargement and ventricular dilation also manifest (16). While a compensatory upregulation of the sarco-endoplasmic reticulum $Ca^{2+}$ ATPase 2 (SERCA2) and its regulator PLN accompanied enhanced ventricular ejection fraction and fractional shortening in *Obscn-ΔIg58/59* animals at 6-months (16), no differences in ventricular myocyte contractility, $Ca^{2+}$ transients, ultrastructure, and fibrotic infiltration were detected (16).

In pursuit of the mechanistic source of atrial arrhythmogenesis and remodeling in *Obscn-ΔIg58/59* mice, we investigated the structural and functional impact of the Ig58/59 deletion in atria at the cellular level. Herein, we show that *Obscn-ΔIg58/59* atria exhibit prominent ultrastructural deficits at the level of the Z-disk and the transverse-axial tubule (TAT) network. Intriguingly, $Ca^{2+}$ cycling alterations occur in *Obscn-ΔIg58/59* atrial cardiomyocytes at 6-months, earlier than in ventricular cardiomyocytes, and progress by 12-months, coinciding with the onset and aggravation of arrhythmia (16). Mechanistically, *Obscn-ΔIg58/59* atrial dysfunction is associated with changes in the expression and phosphorylation profile of T-cap, a sarcomeric titin-binding protein that links transverse-tubules to Z-disks, and junctophilin-2, which spans the cardiac dyad tethering transverse-tubules to the sarcoplasmic reticulum. Collectively, our studies provide insights into the development of atrial remodeling and spontaneous AF that precede ventricular maladaptation.

## Results

### Ultrastructural evaluation of *Obscn-ΔIg58/59* atria reveals prominent Z-disk streaming and misalignment

Our initial characterization of the *Obscn-ΔIg58/59* model revealed spontaneous AF in 6-month-old *Obscn-ΔIg58/59* male animals that progressed in severity by 12-months, accompanied by gross atrial enlargement (16). While fibrosis is a known driver of alterations in electrical conduction and force production in atria (1), *Obscn-ΔIg58/59* atria did not exhibit increased absolute fibrotic content at 6- or 12-months compared to age-matched wild-type **(Fig. 1A).** Interestingly, when normalized to total atrial mass, fibrotic content was significantly decreased in 12-month-old *Obscn-ΔIg58/59* atria compared to age-matched wild-type **(Fig. 1B)**. This indicates that the gross atrial enlargement manifesting at this timepoint (16) is not accompanied by fibrotic deposition, eliminating fibrosis as a possible mechanistic source of arrhythmogenesis.

Our previous biochemical analysis did not indicate differences in the expression levels of obscurin, the binding partners of the Ig58/59 module, titin and PLN, or canonical $Ca^{2+}$ handling proteins between wild-type and *Obscn-ΔIg58/59* atria at 6- or 12-months of age (17). Proteomics/phospho-proteomics analysis, however, exposed extensive changes in the expression and phosphorylation profile of Z-disk associated cytoskeletal proteins and $Ca^{2+}$ cycling regulators in *Obscn-ΔIg58/59* atria at both 6- and 12-months of age, highlighting proteins and phosphorylation events with uncharacterized (patho)physiological roles in the heart (17) that could potentially drive *Obscn-ΔIg58/59* atrial remodeling and dysfunction.

Considering the plethora of deregulated cytoskeletal proteins in *Obscn-ΔIg58/59* atria (17), we evaluated sarcomeric ultrastructure using electron microscopy. Although there were no obvious abnormalities in overall sarcomeric organization, we observed significant Z-disk streaming at both 6- and 12-months **(Fig. 1C-D)**, a common myopathic manifestation characterized by out-of-register Z-disks (18), indicative of lateral myofibrillar misalignment or structural deficiency of the Z-disk itself. Moreover, *Obscn-ΔIg58/59* atria displayed increased variability in Z-disk orientation at 12-months, as determined by the absolute deviation of the Z-disk angle of individual sarcomeres **(Fig. 1E)**. Given that Z-disk alignment remained unaffected in *Obscn-ΔIg58/59* left ventricles (16), these findings indicated that *Obscn-ΔIg58/59* atria are more susceptible to developing structural defects, particularly impacting Z-disk placement and orientation **(Fig. 1F)**. Since the Z-disk is a structural and signaling hub bridging the sarcomere to the extra-sarcomeric cytoskeleton and the neighboring internal membrane systems (i.e., the TAT network and the sarcoplasmic reticulum, SR), these results are consistent with our proteomics study that revealed deregulation of proteins in each of these subcellular compartments (17). It is therefore plausible that the obscurin-Ig58/59 module stabilizes Z-disk-associated protein complexes and supports the overall alignment of adjacent sarcomeres and surrounding structures in atria.

**Atrial cardiomyocytes from sedentary *Obscn-ΔIg58/*59 males exhibit elevated $Ca^{2+}$ spark frequency and age-specific changes in intracellular $Ca^{2+}$ cycling**

The presence of severe AF in *Obscn-ΔIg58/59* mice (16) and the prominent alterations in key regulators of intracellular $Ca^{2+}$ cycling identified in our phospho-proteomic screen (17) prompted us to further evaluate $Ca^{2+}$ homeostasis in atrial cardiomyocytes isolated from sedentary *Obscn-ΔIg58/59* male animals at 6- and 12-months. Cardiomyocytes obtained from *Obscn-*

*ΔIg58/59* atria were moderately enlarged compared to wild-type at 6-months (p=0.08), which progressed to significance by 12-months of age **(Fig. S1A-B)**. To assess intracellular $Ca^{2+}$ cycling dynamics, $Ca^{2+}$ transients were measured in freshly isolated atrial cardiomyocytes. To ensure steady-state $Ca^{2+}$ cycling conditions, atrial cardiomyocytes were electrically paced using field-stimulation at a rate of 1 Hz. At 6-months, *Obscn-ΔIg58/59* atrial cells displayed significantly increased $Ca^{2+}$ transient amplitude and rise time, whereas $Ca^{2+}$ decay time was significantly reduced compared to age-matched wild-type cells **(Fig. 2A-E)**. Conversely, 12-month-old *Obscn-ΔIg58/59* atrial cells exhibited significantly decreased $Ca^{2+}$ transient amplitude and prolonged $Ca^{2+}$ decay, while $Ca^{2+}$ transient rise time was unaffected compared to controls **(Fig. 2A-E)**. Importantly, quantification of the standard deviation (SD) and the coefficient of variation (SI) of the time to half-maximal fluorescence ($TTF_{50}$) assessing the spatial coordination of $Ca^{2+}$ release along the width of cardiomyocytes, demonstrated markedly desynchronized $Ca^{2+}$ transients in *Obscn-ΔIg58/59* atria at both 6- and 12-months **(Fig. 2F-H)**.

SR $Ca^{2+}$ content was also assessed by determining the amount of releasable $Ca^{2+}$ following the application of caffeine after cells had been electrically stimulated at 1 Hz for 30 s to achieve steady-state SR $Ca^{2+}$ loading. The amount of releasable SR $Ca^{2+}$ was significantly elevated in *Obscn-ΔIg58/59* atrial cardiomyocytes at 6-months, as evidenced by increased amplitude of caffeine-induced $Ca^{2+}$ transients, whereas SR $Ca^{2+}$ content was unaffected at 12-months **(Fig. 2I-J)**. Taken together, these changes in intracellular $Ca^{2+}$ cycling align with the natural progression of AF, where 6-month *Obscn-ΔIg58/59* atrial cardiomyocytes show elevated SR load, increased and prolonged $Ca^{2+}$ release, and faster $Ca^{2+}$ decay kinetics, while SR load and kinetics at 12-months are depressed or unchanged. These alterations, along with the dyssynchronous $Ca^{2+}$ release

observed at both timepoints, are consistent with the progressive $Ca^{2+}$ cycling defects typically associated with AF-induced remodeling and maladaptive $Ca^{2+}$ signaling in ACM (1, 19).

Given the abnormalities in atrial $Ca^{2+}$ cycling identified *in vitro* and the episodes of spontaneous AF in *Obscn-ΔIg58/59* animals (16), we next evaluated the frequency and morphology of spontaneous $Ca^{2+}$ sparks in atrial cardiomyocytes. $Ca^{2+}$ sparks are elemental $Ca^{2+}$ release events originating from a single cluster of ryanodine receptors (RyR2) (20, 21). Critically, increased diastolic $Ca^{2+}$ leak resulting from high spontaneous $Ca^{2+}$ spark frequency has been associated with the development of AF and ventricular arrhythmias (20, 22, 23). Indeed, 6-month-old *Obscn-ΔIg58/59* atrial cells exhibited a ~2.6-fold increase in $Ca^{2+}$ spark frequency compared to age-matched controls **(Fig. 3A, C)**. Further assessment of $Ca^{2+}$ spark morphology revealed significantly increased spark amplitude, full width at half-maximum (FWHM), full-duration at half-maximum (FDHM), spark mass, time to peak, and Tau (exponential time constant of spark decay) with no alterations in the maximum steepness of spark upstroke in 6-month-old *Obscn-ΔIg58/59* atrial cells compared to wild-type **(Fig. 3D and F-I; Fig. S1C-G)**. Strikingly, by 12-months, *Obscn-ΔIg58/59* atrial cardiomyocytes exhibited a ~4.0-fold increase in $Ca^{2+}$ spark frequency compared to age-matched controls **(Fig. 3B-C)**. Morphologically, $Ca^{2+}$ sparks originating from 12-month-old *Obscn-ΔIg58/59* atrial cells displayed decreased amplitude and spark mass, with no significant alterations in FWHM, FDHM, time to peak, maximum steepness of spark upstroke, or in Tau **(Fig. 3E-I; Fig. S1C-G)**.

Collectively, these findings indicate increased intracellular $Ca^{2+}$ load in 6-month *Obscn-ΔIg58/59* atrial cardiomyocytes, where elevated SR $Ca^{2+}$ levels are associated with augmented

$Ca^{2+}$ transients and more frequent and larger $Ca^{2+}$ sparks. Conversely, by 12-months, *Obscn-ΔIg58/59* atrial cells exhibit depressed $Ca^{2+}$ transients and kinetics in the absence of elevated SR $Ca^{2+}$ load along with the presence of more frequent but lower magnitude $Ca^{2+}$ sparks. Importantly, this increased spontaneous $Ca^{2+}$ spark activity at both timepoints implies a persistent $Ca^{2+}$ leak from the SR that could promote AF in *Obscn-ΔIg58/59* mice.

**The transverse-axial tubule (TAT) network is disrupted in *Obscn-ΔIg58/59* atria**

The presence of progressive structural abnormalities at the level of the Z-disk along with age-specific alterations in $Ca^{2+}$ cycling dynamics and $Ca^{2+}$ spark frequency in *Obscn-ΔIg58/59* atrial cells prompted us to investigate TAT membrane architecture using super-resolution microscopy. Freshly isolated live atrial cardiomyocytes were stained with di-8-ANEPPS, a fluorescent lipophilic plasma membrane marker that is commonly utilized to visualize the transverse-tubule system (24, 25). Quantification of the length and orientation of the TAT network demonstrated a significant reduction in TAT density in *Obscn-ΔIg58/59* atria at both 6- and 12-months compared to age-matched wild-type **(Fig. 4A-D)**, with no significant changes in directionality **(Fig. 4E-G)**. The observed structural deterioration of the TAT network in *Obscn-ΔIg58/59* atria likely contributes to impaired CICR resulting in asynchronous $Ca^{2+}$ release from the SR and consequent arrhythmogenicity at both 6- and 12-months.

**The expression and phosphorylation status of T-cap is altered in *Obscn-ΔIg58/59* atria**

To mechanistically interrogate the profound structural and $Ca^{2+}$ cycling changes that we discovered in *Obscn-ΔIg58/59* atria, we utilized our prior phospho-proteomics screen as a guide (17). Given the significant alterations in both Z-disk and TAT morphology in *Obscn-ΔIg58/59*

243 atria, we focused our investigation on T-cap, for which our phospho-proteomics analysis indicated
244 altered phosphorylation in 12-month old *Obscn-ΔIg58/59* atria (17). T-cap binds to titin's extreme
245 $NH_2$-terminal Ig1/2 domains located at the Z-disk in proximity to titin-Ig9/10 encompassing the
246 binding site for obscurin-Ig58/59. T-cap at the Z-disk is postulated to support the structural
247 integrity and physical association of the sarcomere with the transverse-tubule network by
248 interacting with ion channel accessory subunits (26-29), in addition to regulating responses to
249 biomechanical and hemodynamic stress (30, 31). Endogenous T-cap exists in a constitutively bi-
250 phosphorylated state at residues Ser157 and Ser161 (28). Although neither the hierarchy nor the
251 function of each phosphorylation event is known, it has been postulated that the phosphorylation
252 status of T-cap may regulate its susceptibility to proteasomal degradation and influence the
253 integrity of the transverse-tubule network in ventricular myocardium (28, 31, 32).
254
255 We therefore investigated the levels, phosphorylation profile, and localization of T-cap in
256 *Obscn-ΔIg58/59* atria. At 6-months, T-cap expression was significantly increased in *Obscn-*
257 *ΔIg58/59* atria compared to age-matched controls, whereas T-cap levels were unaltered at 12-
258 months **(Fig. 5A-B)**. Due to the lack of commercial antibodies for pSer157 and pSer161, we
259 utilized Phos-tag™ acrylamide gels to separate the different T-cap phospho-species. We detected
260 a bi-phosphorylated (2P) species, two mono-phosphorylated forms ($1P_1$ and $1P_2$), and non-
261 phosphorylated T-cap (0P; **Fig. 5C)**. Although the $1P_1$ and $1P_2$ species harbor the same number of
262 phosphates, they exhibit distinct mobilities, since Phos-tag electrophoresis may differentially delay
263 the migration of proteins depending not only on the number but also the location of phosphate
264 groups (33). Following normalization to total T-cap levels, we did not observe a significant
265 difference in the abundance of any phospho-species between wild-type and *Obscn-ΔIg58/59* atria

at 6-months **(Fig. 5D)**. However at 12-months, *Obscn-ΔIg58/59* atria exhibited a significant upregulation of the 2P species accompanied by a corresponding decrease in the lower molecular weight $1P_1$ species compared to age-matched wild-type **(Fig. 5D-E)**; a finding that is in agreement with the reduced phosphorylation levels of Ser161 detected in our phospho-proteomics screen (17). Despite its altered expression at 6-months or phosphorylation at 12-months, T-cap was properly localized to sarcomeric Z-disks in *Obscn-ΔIg58/59* atria at both 6- and 12-months **(SFig. 2)**.

Previous studies have postulated that T-cap expression is augmented as an adaptive response to sustained cardiac stress (31). To determine whether dysregulation of T-cap expression and phosphorylation is a direct consequence of the Ig58/59 deletion or secondary to maladaptive structural and electrical remodeling, we examined T-cap and phospho-T-cap levels in the atria of 3.5-month-old *Obscn-ΔIg58/59* mice, at a stage immediately prior to the onset of arrhythmia, remodeling, and dysfunction (16). There was no significant difference in total T-cap expression between genotypes at 3.5-months of age **(Fig. 5A-B)**. However, quantification of T-cap phosphorylation via PhosTag™ immunoblotting revealed a significant increase in 2P T-cap and a corresponding decrease in 1P1 T-cap in 3.5-month-old *Obscn-ΔIg58/59* atria compared to age-matched controls, reminiscent of the T-cap phospho-spectra in 12-month *Obscn-ΔIg58/59* atria **(Fig. 5C-D)**. The non-phosphorylated T-cap (0P) species was not reliably detected in lysates from 3.5-month-old atria and was therefore not included in quantifications. Thus, the altered phosphorylation profile of T-cap appears to be an early consequence of the Ig58/59 deletion, that becomes obscured at 6-months due to a compensatory up-regulation of total T-cap and is re-exposed and exacerbated at 12-months. Collectively, these findings indicate that deletion of Ig58/59 leads to intrinsic molecular changes in the phosphorylation profile of T-cap, possibly

289 contributing to the maladaptive remodeling of the Z-disk and TAT membranes in *Obscn-ΔIg58/59*
290 atria.
291
292 **The expression of JPH2 is altered in *Obscn-ΔIg58/59* atria**
293 Given the substantial degradation of TAT structures in *Obscn-ΔIg58/59* atria, we next
294 queried whether Ig58/59 deletion altered the SR network, too. Previous analysis of *Obscn-*
295 *ΔIg58/59* atrial lysates revealed no changes in the expression of SR proteins SERCA, RyR2, or
296 sAnk1 (17). Similarly, sAnk1 localization was nondifferent in *Obscn-ΔIg58/59* atria compared to
297 wild-type controls, suggesting that the SR structure is unaffected by Ig58/59 ablation **(SFig. 3)**.
298 However, we identified increased expression of the full-length form of junctophilin 2 (JPH2) in
299 *Obscn-ΔIg58/59* atria at 12-months **(Fig. 5F-G)**. JPH2 fastens the transverse-tubules to the SR in
300 cardiomyocytes and dictates the dimensions of the dyadic cleft (34). In fact, JPH2 downregulation
301 is a common corollary of TAT remodeling in heart disease (35). Yet, calpain cleavage of JPH2
302 yields an ~75 kDa N-terminal fragment, JPH2 NT1, that is commonly upregulated under
303 conditions of cardiac stress (36, 37), though not following Ig58/59 ablation **(Fig. 5H)**. JPH2 NT1
304 translocates to the nucleus where it acts as a cardioprotective transcription factor, governing genes
305 involved in hypertrophy, fibrosis, and inflammation (37). As there is a necessary trade-off between
306 the TAT-tethered population of JPH2 critical for excitation-contraction coupling and the nuclear
307 pool of cleaved JPH2 NT1, a relative increase in the non-cleaved form of JPH2 in 12-month
308 *Obscn-ΔIg58/59* atria may act as an adaptive measure to reinforce remaining dyads at the expense
309 of inducing a protective gene program. In agreement, despite the loss of TATs in Obscn-ΔIg58/59
310 atria, we detected no changes in JPH2 localization via immunofluorescence **(SFig. 4)**. In sum,
311 although the SR appears unchanged in *Obscn-ΔIg58/59* atria, by 12-months of age there is notable

312 dysregulation of the proteins involved in linking TATs to both the sarcomeric cytoskeleton (T-
313 cap) and the SR (JPH2).

## Discussion

Our current findings in combination with our prior proteomics study (17) provide insights into the cellular and molecular alterations underlying atrial remodeling and arrhythmia in *Obscn-ΔIg58/59* mice **(Fig. 6)**. Specifically, our ultrastructural analysis indicated that deletion of the Ig58/59 module significantly affected the orientation and alignment of Z-disks in atria. In accordance with this, our proteomic analysis of *Obscn-ΔIg58/59* atria exposed extensive alterations in the expression and/or phosphorylation status of Z-disk associated cytoskeletal and regulatory proteins (17). The Z-disk is a critical nexus where the sarcomeric cytoskeleton interfaces with surrounding cellular structures, including internal membrane systems, the extra-sarcomeric cytoskeleton, intercalated discs, costameres/sarcolemma, and the TAT network (38, 39). Consequently, the Z-disk simultaneously governs a diverse array of cellular processes such as sarcomeric assembly, force production, cell adhesion, intracellular $Ca^{2+}$ homeostasis, and metabolism, while serving as a hotspot for mechanosensitive signaling pathways (38, 39). Thus, perturbations in Z-disk-associated protein complexes (17) likely render *Obscn-ΔIg58/59* atria susceptible to routine mechanical stress, worsening Z-disk alignment and sarcomeric topography.

Accordingly, we identified age-specific alterations in the expression (6-months) and phosphorylation (3.5- and 12-months) status of the Z-disk localized, titin-binding protein T-cap in *Obscn-ΔIg58/59* atria. Prior to the onset of arrhythmia and whole organ dysfunction (16), we observed reduced mono-phosphorylated (1P1) and increased bi-phosphorylated (2P) T-cap species, suggesting that T-cap altered phosphorylation develops as a direct consequence of Ig58/59 deletion, likely contributing to the initiation of Z-disk destabilization in *Obscn-ΔIg58/59* atria. By 6-months, total T-cap expression is increased in *Obscn-ΔIg58/59* atria, which may be an adaptation to insulate the Z-disk and associated structures from excessive mechanical strain. Such a notion

would be in agreement with previous studies documenting that sustained exposure to cardiac stress prompts up-regulation of T-cap expression (31). While 12-month *Obscn-ΔIg58/59* atria do not exhibit this same compensatory increase in T-cap levels, we observed a reduction in a single mono-phosphorylated T-cap species, likely pSer161 (17), with a complementary increase in bi-phosphorylated T-cap, akin to what was found in sedentary 3.5 month-old *Obscn-ΔIg58/59* atria. Thus, our findings indicate that deletion of obscurin-Ig58/59 induces alterations in the phosphorylation profile of the Z-disk-associated protein, T-cap, which is concealed at 6-months due to adaptive upregulation of total T-cap and intensified at 12-months when Z-disk architecture and TAT network density appear dramatically deteriorated.

The obscurin Ig58/59 module interacts with the $NH_2$-terminal Ig9/10 domains of titin at the Z-disk within relative proximity to T-cap's binding site on titin Ig1/2 region (14, 29). While localization of T-cap to sarcomeric Z-disks appeared unaffected in *Obscn-ΔIg58/59* atria, it is tempting to speculate that disruption of obscurin/titin binding via deletion of Ig58/59 may indirectly impact T-cap association with titin-Ig1/2. Alternatively, it may influence the ability of obscurin and titin to serve as molecular scaffolds for local kinase and phosphatase networks that regulate T-cap's phosphorylation. Along these lines, our phospho-proteomics analysis revealed many Z-disk-localized and/or actin-associated cytoskeletal proteins with deregulated phosphorylation including plectin, cortactin, synaptopodin 2-like, LIM-domain binding protein 3 (ZASP), myozenin, and synemin, in addition to T-cap (17). Intriguingly, our proteomics results also revealed an upregulation of $Ca^{2+}$/calmodulin-dependent kinase II (CaMKII) phosphorylation at Thr331 in 12-month *Obscn-ΔIg58/59* atria (17). Although the significance of this phosphorylation event is not yet understood, Thr331 resides within the CaMKII linker region along

with a handful of other phospho-sites that putatively govern CaMKII autophosphorylation and activation (40). Given that T-cap Ser157 and Ser161 are substrates of CaMKII (28), it is possible that CaMKII Thr331 phosphorylation in 12-month *Obscn-ΔIg58/59* atria could contribute to excess T-cap bi-phosphorylation in *Obscn-ΔIg58/59* atria.

To date, the precise function of T-cap bi-phosphorylation remains undefined, although it has been suggested that constitutive phosphorylation of Ser157 and Ser161 regulates the overall stability of T-cap. Wirianto *et al.* previously reported that dually phospho-ablated exogenous T-cap is protected against proteasomal degradation when overexpressed in 293T cells (32). Contrary to this, Lewis *et al.* observed a robust decrease in ventricular, dually phospho-ablated, endogenous T-cap levels in the respective knock-in mouse line (31). Given these discrepant findings along with the difficulty in disentangling the downstream effects of T-cap loss versus phospho-ablation, and the lack of knowledge regarding the potentially distinct functions of pSer157 and pSer161, our current understanding of the consequences of T-cap phosphorylation remains limited. Despite this lingering ambiguity in the literature, a clear link has been established between T-cap expression, T-cap phosphorylation, TAT structure, and the synchronicity of $Ca^{2+}$ release (27, 28). Accordingly, ventricular myocytes isolated from T-cap knock-out mice exhibit a progressive loss of transverse-tubule membranes, dyssynchronous $Ca^{2+}$ release, and frequent $Ca^{2+}$ sparks as they age (27). Moreover, overexpression of phospho-ablated T-cap, lacking both pSer157 and pSer161, in rat ventricular myocytes leads to disordered, but not diminished, transverse-tubules along with prolonged, desynchronized, $Ca^{2+}$ release. Importantly, our current findings demonstrate that the putative roles of T-cap in regulating the integrity of the transverse-tubule network and the synchronicity of $Ca^{2+}$ release also apply to atrial cardiomyocytes.

The significant depletion of the TAT system in *Obscn-ΔIg58/59* atria may implicate a reduction in aligned RyR2/LTCC junctional complexes that facilitate proper CICR. Just as 'orphaned' (i.e. misaligned) RyR2 clusters are known to produce arrhythmogenic $Ca^{2+}$ release in ventricular myocytes in heart failure (41), TAT depletion has been detected in atrial myocytes derived from sheep with AF (42). Relatedly, seminal work by Brandenburg *et al* (43) demonstrated the importance of the TAT system and its orientation (axial versus transverse) for synchronous $Ca^{2+}$ release in atrial myocytes. Specifically, these authors showed that atrial myocytes adapt to hypertrophy by increasing axial TAT elements thereby maintaining $Ca^{2+}$ release despite maladaptive remodeling (43). No such compensation of the TAT system occurred in our model, despite upregulation of the junctional protein JPH2 at 12-months, which has been shown to restore TAT regression and enhance LTCC recruitment elsewhere (35). Consequently, it seems the structural deficits afflicting Z-disks and TATs in *Obscn-ΔIg58/59* atria, driven by extensive alterations in the expression and phosphorylation of Z-disk associated proteins including T-cap, are too systemic to be overcome by late-stage adaptive mechanisms (17). Instead, the progressive deterioration of the TAT network in *Obscn-ΔIg58/59* atrial cardiomyocytes coincides with the development and advancement of arrhythmogenic $Ca^{2+}$ handling dynamics. We thus posit that TAT depletion constitutes an important, emerging mechanism of $Ca^{2+}$-based arrhythmogenicity and associated atrial cardiomyopathy.

*Obscn-ΔIg58/59* male mice exhibit episodes of spontaneous arrhythmia reminiscent of human AF, with the frequency and severity of these episodes increasing as the mice age from 6- to 12-months (16). In line with this, we witnessed progressive abnormalities in $Ca^{2+}$ cycling kinetics, $Ca^{2+}$ sparks, and SR $Ca^{2+}$ content. Specifically, at 6-months we observed increased SR

$Ca^{2+}$ load associated with prolonged, amplified, and desynchronized $Ca^{2+}$ transients that were accompanied by larger and more frequent $Ca^{2+}$ sparks. While desynchronized $Ca^{2+}$ release and elevated $Ca^{2+}$ spark frequency persisted through 12-months, $Ca^{2+}$ release amplitude and kinetics were substantially depressed. These changes are consistent with the natural progression of AF from paroxysmal to permanent (44). Indeed, previous work in atrial myocytes isolated from patients with paroxysmal AF revealed an increase in SR $Ca^{2+}$ load akin to the phenotype of 6-month-old *Obscn-ΔIg58/59* atria (45). Further, atrial myocytes isolated from a patient with chronic AF exhibited no alterations in SR $Ca^{2+}$ load, similar to our findings in 12-month-old *Obscn-ΔIg58/59* mice (46). Promiscuous $Ca^{2+}$ spark activity may result from excessive RyR2 leak, frequently linked to hyper-phosphorylation of RyR2 at Ser2808 and Ser2814. Our phospho-proteomic analysis of 12-month *Obscn-ΔIg58/59* atria revealed increased phosphorylation of RyR2 at Ser2811, a CaMKII and PKA-sensitive site within the "phosphorylation hotspot" not yet fully characterized but theorized to augment channel open probability (17, 47, 48). We also detected reduced phosphorylation of histidine rich $Ca^{2+}$ binding protein (HRC) – a regulator of SR $Ca^{2+}$ uptake, storage, and release – at another functionally uncharacterized site, Ser272, in *Obscn-ΔIg58/59* atria at 12-months (17). Collectively, our data intimates a mechanism where deregulated $Ca^{2+}$ dynamics in *Obscn-ΔIg58/59* atria develop secondary to molecular alterations and structural deficits, which is corroborated by our proteomic screen in *Obscn-ΔIg58/59* atria (17).

Ventricular and atrial tissues comprising the different chambers of the heart possess inherent differences in cellular morphology, TAT membranes, and $Ca^{2+}$ cycling (49, 50). Consistent with this, our current study provides evidence of distinct pathophysiological alterations in the atria versus ventricles (16) due to obscurin-Ig58/59 deletion. In particular, while the

pathological manifestations of Ig58/59 ablation in ventricles are regulatory in nature (i.e., de-regulated $Ca^{2+}$ cycling due to changes in key $Ca^{2+}$ cycling proteins in the absence of ultrastructural alterations) (16), *Obscn-ΔIg58/59* atria exhibit discrete and antecedent structural and signaling deficits (16). Critically, enhanced ventricular contractility in 6-month *Obscn-ΔIg58/59* male hearts, evidenced by increased ejection fraction and fractional shortening in the absence of ventricular myocyte abnormalities (16), implies elevated pressure on the atria during systole. This excess hemodynamic strain may contribute to the structural and functional remodeling of atrial cardiomyocytes in *Obscn-ΔIg58/59* males. However, our biochemical analysis revealed alterations in T-cap phosphorylation in *Obscn-ΔIg58/59* atria as early as 3.5-months of age, prior to the development of ventricular remodeling at 6-months. We therefore postulate that obscurin and/or Ig58/59 may serve specialized roles in different cardiac chambers, rendering the atria particularly vulnerable to progressive pathophysiological remodeling due to Ig58/59 ablation.

Our current findings situate the *Obscn-ΔIg58/59* mouse model as one of few surrogates for human ACM, featuring atrial fibrillation, atrial dilation, and progressive, sex-dependent pathogenesis. Not only do *Obscn-ΔIg58/59* male atria mimic the morphological and electrophysiological consequences of this disease, but they also mirror the cellular and molecular hallmarks of ACM Class 1, characterized by principal changes to the cardiomyocyte driven by genetic factors that culminate in lone AF in the absence of substantial fibrosis (1). In other genetic models featuring AF, the origin and accelerant of arrhythmogenesis is not always explicit. In the *Obscn-ΔIg58/59* mouse model, we demonstrate a clear chronology wherein the onset and advancement of AF in males coincides with the progressive ultrastructural deficits and $Ca^{2+}$ cycling dysfunction of atrial cardiomyocytes. Just as *Obscn-ΔIg58/59* females are insulated against

453 atrial remodeling and AF, women commonly incur AF later than men, often manifesting after
454 menopause (51). The prominent sex differences in AF incidence in our model are likely driven by
455 sex hormones, although estrogen, progesterone, and testosterone exert complex effects on ECG
456 morphology and arrhythmia prevalence (51, 52). Importantly, not all animal models of AF
457 recapitulate the sex bias seen in human AF, but the *Obscn-ΔIg58/59* model could be utilized to
458 elucidate sex-specific arrhythmogenic processes (53, 54).
459
460 Taken together, our past (17) and present studies reveal that deletion of obscurin-Ig58/59
461 in atria disrupts the expression and phosphorylation state of T-cap among other Z-disk-associated
462 structural and signaling proteins. Using ultrastructural evaluation, high resolution imaging of
463 intracellular $Ca^{2+}$ dynamics, and live-cell super resolution microscopy of TAT membranes, we
464 show that deletion of the obscurin Ig58/59 module underlies adverse structural remodeling of Z-
465 disks and TAT membranes in atrial cardiomyocytes that likely fuel $Ca^{2+}$ deregulation and
466 arrhythmia. These findings provide mechanistic insights into the development of atrial remodeling
467 and arrhythmogenesis and establish the *Obscn-ΔIg58/59* line as a genetic model of ACM where
468 atrial pathology develops prior to ventricular maladaptation.

## Methods

*Sex as Biological Variable*

The current study focuses on the functional and molecular deficits in *Obscn-ΔIg58/59* male atria. We observed robust, progressive arrhythmias in *Obscn-ΔIg58/59* males, with 50% and 83% developing arrhythmia at 6- and 12-months, respectively, of which 37.5% and 83% experience AF (16). In contrast, 33% of 6-month and 37% of 12-month-old *Obscn-ΔIg58/59* females exhibited one or more forms of arrhythmia under sedentary conditions (16). Interestingly, AF incidence actually declined over time in *Obscn-ΔIg58/59* females, as 33% versus 12% displayed AF at 6- and 12-months, respectively. Female sex-hormones, particularly estrogen, most likely insulate *Obscn-ΔIg58/59* females from atrial remodeling and electrical abnormalities. Consequently, the current study focuses on the molecular mechanisms of atrial pathogenesis in *Obscn-ΔIg58/59* male atria.

*Obscn-ΔIg58/59 constitutive deletion mice*

The *Obscn-ΔIg58/59* constitutive deletion model was generated as described previously (GenOway, Lyon, France) (16). Genotypes were confirmed by polymerase chain reaction (PCR) utilizing two distinct primer sets (16). All experiments were performed with homozygous male *Obscn-ΔIg58/59* animals and age-matched male wild-type. Backcrossing of the *Obscn-ΔIg58/59* colony is performed every 5-10 generations to protect against genetic drift.

*Hydroxyproline assay*

Hydroxyproline content was quantified from flash-frozen cardiac tissue as described previously (13, 16). Briefly, right and left atria were combined and boiled overnight in 0.2 mL of

6 mol/L HCl at 110 ˚C. The hydrolyzed tissue was diluted 1:16 in isopropanol, combined 2:1 with Reagent A (62 mmol/L chloramine-T, 0.56 mol/L sodium acetate, 0.14 mol/L citric acid, 0.35 mol/L NaOH, and 30.8% (v/v) isopropanol in water), and incubated at room temperature for 5 min. Samples were further diluted 1:4 in Reagent B (0.35 mol/L p-dimethylbenzeldehyde, 17.55% (v/v) ethanol, and 1.19% (v/v) sulfuric acid in isopropanol), incubated at 55 ˚C for 1 hour, and quenched on ice. Absorbance values were obtained at 558 nm and hydroxyproline content was calculated using a standard curve and presented as either the absolute hydroxyproline concentration (μM) or normalized to input atrial tissue mass (μM/mg).

*Electron microscopy*

Atrial samples were prepared for electron microscopy following methods for mega metal staining (55). Briefly, atria isolated from 6- and 12-month-old wild-type and *Obscn-ΔIg58/59* mice were fixed in 2% paraformaldehyde, 2.5% glutaraldehyde, and 0.1 mol/L PIPES buffer (pH 7.4), washed with 0.1 mol/L PIPES buffer and postfixed for 60 min in 0.75% potassium ferrocyanide and 1% osmium tetroxide in 0.1M PIPES buffer, followed by washing with water and 20 min treatment with 1% freshly prepared thiocarbohydrazide solution at room temperature. After extensive washing with water, samples were stained with 1% osmium tetroxide for 60 min, washed in water and left in 1% uranyl acetate overnight at 4ºC. Samples were then stained with lead aspartate at 60ºC for 30 min, washed with water and dehydrated using serial graded ethyl alcohol (30%, 50%, 70%, 80%, 90% and 100%) and 100% acetone. Samples were then embedded in Durcupan resin following the manufacturer's recommendation (Electron Microscopy Sciences, PA, USA). Ultrathin sections at 70 nm thickness were cut on a Leica UC6 ultramicrotome (Leica Microsystems, Inc., Bannockburn, IL), and examined under a Tecnai T12 transmission electron

515 microscope (Thermo Fisher Scientific, Hillsboro, Oregon) operated at 80 kV. Images were
516 acquired with an AMT bottom mount CCD camera and AMT600 software (Advanced Microscopy
517 Techniques, Woburn, MA). All samples were prepared and imaged at the Electron Microscopy
518 Core Imaging Facility of the University of Maryland Baltimore.
519
520 Z-disk streaming was evaluated by annotating the presence or absence of streaming in a
521 subset of images taken at 3200X magnification (10 ± 3 images per animal at 6-months, 15 ± 3
522 images per animal at 12-months). A two-sided Fisher's exact test (GraphPad Prism software ver.
523 5.00, San Diego, CA) was used to compare the proportion of images containing Z-disk streaming
524 between age-matched wild-type and *Obscn-Δig58/59* mice. Variability in Z-disk orientation was
525 evaluated by calculating the absolute deviation of the Z-line angle (measured with ImageJ) for all
526 sarcomeres visible in two representative images per animal (taken at 3200X magnification;
527 approximately 20-80 sarcomeres were analyzed per image).
528
529 *Atrial cardiomyocyte isolation*
530 Atrial cardiomyocytes were isolated from 6- and 12-month-old mice using a modified
531 Langendorff perfusion system as described previously (16, 24, 56, 57). Mice were anesthetized
532 using 3% isoflurane in oxygen and injected intraperitoneally with 108U heparin. Dissected hearts
533 were placed directly in digestion buffer (DB; 133 mmol/L NaCl, 5 mmol/L KCl, 2 mmol/L
534 $MgCl_2$•$6H_2O$, 1.2 mmol/L $KH_2PO_4$, 6 mmol/L taurine, 6 mmol/L creatine, 10 mmol/L glucose, 10
535 mmol/L HEPES, pH 7.4) containing 0.4 mmol/L EGTA (DB-EGTA) on ice. Hearts were
536 cannulated through the aorta and perfused in retrograde with DB-EGTA for 2 min and
537 subsequently perfused with DB-Enzymes solution containing 4 mg/ml bovine serum albumin

(BSA), 0.3 mmol/L $CaCl_2$, 1 mg/ml collagenase (Worthington), 0.04 mg/ml trypsin (Sigma-Aldrich), and 0.04 mg/ml protease type XIV (Sigma P5147) for 5 min at 37 $^0$C. Atria were separated from ventricles, minced, and subjected to additional digestion in DB-Enzymes for 5 min at 37 $^0$C. Enzymatic digestion was terminated by transferring atrial tissues to DB containing 4 mg/ml BSA, 3.2 mg/ml 2,3-butanedione monoxime (BDM), and 0.2 mmol/L $CaCl_2$ where myocytes were mechanically dispersed by trituration with a Pasteur pipette. Only myocytes that exhibited appropriate morphology (rod-shaped with clear cross-striations) and were responsive to electrical stimulation were used for downstream experimentation. Given the technical difficulties involved in isolating high-quality, primary atrial cardiomyocytes from a miniscule amount of tissue (<10 mg), any atria yielding at least two healthy myocytes was included in analyses. Cells isolated from the same atria are similarly colored within figures, and the number of cells analyzed per atrial sample is indicated in the corresponding figure legends.

*$Ca^{2+}$ imaging and analysis*

$Ca^{2+}$ imaging in atrial myocytes was performed as described previously (24). Isolated cardiomyocytes were plated in chambers coated with ECM gel (e1270, Sigma-Aldrich) and mounted on a Nikon Eclipse Ti inverted microscope with a 60X Oil 1.4 NA objective. Cells were loaded for 20 min with 1 μmol/L fluo-4-acetoxymethyl ester (Fluo-4-AM; ThermoFisher F14201) followed by de-esterification for 10 min. Subsequently, cells were brought to physiological $Ca^{2+}$ by perfusion with normal Tyrode's solution (NT; 135 mmol/L NaCl, 5.4 mmol/L KCl, 1 mmol/L $MgCl_2$•$6H_2O$, 0.33 mmol/L $NaH_2PO_4$, 11 mmol/L glucose, 5 mmol/L HEPES, 1.8 mmol/L $CaCl_2$, pH 7.4). $Ca^{2+}$ transients were measured during 1 Hz external field stimulation (2 ms, 20 V; MyoPacer, IonOptix) using the 488 nm laser line of a confocal laser scanning microscope (Nikon

561 A1R). Line scans (1.872 ms/line) were collected in transverse orientation for 30 seconds. $Ca^{2+}$
562 sparks were imaged for 30 seconds in quiescent atrial myocytes preceded by 30 seconds of external
563 field stimulation at 1 Hz to ensure steady-state SR $Ca^{2+}$ loading. SR $Ca^{2+}$ content was measured
564 by rapid application of 10 mmol/l caffeine to quiescent cells preceded by steady-state external field
565 stimulation at 1 Hz for 30 seconds. Field stimulation was subsequently restarted at 1 Hz to ensure
566 that all releasable $Ca^{2+}$ had been depleted from the SR.
567
568 The resulting electrically- or caffeine-induced $Ca^{2+}$ transients were analyzed offline using
569 ImageJ and Clampfit analysis software v11.1 (Molecular Devices, San Jose, CA). $Ca^{2+}$ transients
570 were analyzed by averaging the Fluo-4 signal across the entire cell's width, and are presented as
571 background-subtracted, normalized fluorescence ($F/F_o$, arbitrary units). The delay of $Ca^{2+}$ release
572 across the transverse axis of the cardiomyocyte was evaluated using a custom-made Python script
573 (58) quantifying the time to half maximal fluorescence ($TTF_{50}$) for each pixel. The dispersion of
574 delay values (i.e., standard deviation, SD) and the coefficient of variation (SD/mean) for each
575 transient represents $Ca^{2+}$ release synchrony. $Ca^{2+}$ spark frequency and morphology was assessed
576 from concatenated line scan images using ImageJ Sparkmaster plugin (59). Spark mass was
577 calculated as: amplitude x 1.206 x FWHM $^3$ as described previously (60). 3-Dimensional surface
578 plot renderings of $Ca^{2+}$ sparks were generated with ImageJ.
579
580 *Transverse-axial tubule (TAT) imaging and analysis*
581 Transverse-axial tubule imaging was carried out with a Zeiss LSM 880 confocal microscope
582 equipped with an Airyscan super resolution imaging module using a 63/1.40 Plan-Apochromat Oil
583 differential interference contrast M27 objective lens (Zeiss) as described previously (61). Freshly

isolated atrial cardiomyocytes were loaded with the membrane dye di-8 ANEPPS (5 μmol/L) and imaged within 1.5 h after cell isolation as described previously (24). Only structurally intact atrial cardiomyocytes with continuous cell membranes were selected for analysis. For transverse-axial tubule (TAT) analysis, the NIH open-source Fiji platform was used (62). Cell interior regions of interest (ROIs) were drawn with the polygon selection tool such that di-8-ANEPPS signal on the cardiomyocyte surface was excluded. These ROIs were processed using a FIJI macro derived from (63) and optimized for atrial TAT networks in older animals:

```
run("Add to Manager");
run("Enhance Contrast", "saturated=0.35");
run("Measure");
run("Duplicate…", " ");
run("Clear Outside");
run("Subtract Background…", "rolling=5");
run("8-bit");
run("Statistical Region Merging", "q=100 showaverages");
setThreshold(20, 255);
run("Convert to Mask");
run("Skeletonize (2D/3D)");
run("Directionality", "method=[Fourier components] nbins=180 histogram=-45 display_table");
run("Analyze Skeleton (2D/3D)");
```

Branch lengths, branch counts, junction counts, directionality histograms, ROI areas, and micron to pixel ratios were saved in excel files for each cell. These files were batch analyzed using a custom Matlab script (25, 64). The proportion of transverse and axial tubules in each cell was calculated from the area under the curve of the directionality histograms at 90º ± 2º (transverse orientation) and 0º ± 2º (axial orientation).

*Lysate preparation, standard and Phos-tag™ gel electrophoresis, and immunoblotting*

Atrial lysates were generated as described previously (16, 17) from mice at 3-4 (denoted as 3.5 in the text), 6, or 12-months of age. Briefly, flash frozen right and left atrial tissues were combined and ground into a fine powder using a glass Dounce homogenizer submerged in liquid

nitrogen. The ground tissues were incubated at -20 ºC for 20 min and then solubilized in a 1:1 mixture of urea-thiourea lysis buffer (8 mol/L urea, 2 mol/L thiourea, 3% SDS, 0.05 mol/L tris-HCl, 0.03% bromophenol blue, 0.075 mol/L dithiothreitol, pH 6.8) and 50% glycerol supplemented with protease and phosphatase inhibitors (Halt Protease and Phosphatase Inhibitor Cocktail, Thermo Fisher Scientific, Waltham, MA) in a 60 ºC water bath. Following centrifugation, the supernatant was collected, aliquoted, and flash frozen in liquid nitrogen. Lysates were thawed at 55 ºC for 5 min and separated either by standard SDS-polyacrylamide gel electrophoresis (SDS-PAGE) as described previously (16, 17) or Phos-tag™ gel electrophoresis. For Phos-tag™ gel electrophoresis lysates were separated for 3 hours (30 mA/gel) on 12% polyacrylamide gels supplemented with 50 μmol/L Phos-tag™ acrylamide according to the $Zn^{2+}$ Phos-tag™ (FUJIFILM Wako Chemicals, Richmond, VA) SDS-PAGE protocol according to the manufacturer's instructions. Standard SDS-PAGE and Phos-tag™ gels were transferred to nitrocellulose membranes, blocked in 3% BSA, and probed with primary antibodies against T-cap (1:1000; ab133646; Abcam), JPH2 (1:1000; INV-405300; Invitrogen), glyceraldehyde 3-phosphate dehydrogenase (GAPDH; 1:15000; G8795; Millipore), or α-actinin (1:1000; A7811; Sigma-Aldrich). Horseradish peroxidase (HRP)-conjugated secondary antibodies (goat anti-mouse IgG, CST-7076S, or goat anti-rabbit IgG, CST-7074S; 1:3000; Cell Signaling Technology) and chemiluminescent reagents (Pierce, ECL) were applied to visualize immunoreactive bands. Total T-cap was quantified via densitometry (ImageJ) and normalized to GAPDH or α-actinin as a loading control. The relative abundance of each T-cap phospho-species was determined by dividing the relative intensity of each species by the summed intensity of all species for a given sample and is presented as the percent of total T-cap.

*Immunostaining and confocal microscopy*

Frozen cardiac sections were prepared as described previously (16). In brief, following perfusion and fixation in 2% paraformaldehyde (PFA) in phosphate-buffered saline (PBS), dissected atria were embedded in 7.5% gelatin and 15% sucrose in PBS and frozen with 2-methylbutane. Samples sectioned at a thickness of 12 μm were permeabilized with 0.1% (T-cap) or 0.3% (JPH2 and sAnk1) Triton X-100 in PBS, blocked in 1 mg/ml BSA with 1 mmol/L sodium azide in PBS (T-cap) and 1% goat serum (JPH2 and sAnk1), and incubated with primary antibodies targeting T-cap (1:250; ab133646; Abcam), JPH2 (1:100; INV-405300; Invitrogen), or sAnk1 (1:200; ARP42566_T100; Aviva). Samples were then incubated with Alexa Fluor™ 488 goat anti-rabbit (1:300; A11034, Invitrogen) secondary antibody for 2 hours, stained with Alexa Fluor™ 647 phalloidin (1:30; A22287, Invitrogen) for 30 minutes, and mounted with VECTASHIELD mounting medium (Vector Laboratories, Burlingame, CA). Immunostained sections were analyzed under a Nikon Spinning Disc confocal microscope at the UMSOM Confocal Microscopy Facility. The brightness/contrast of images was adjusted uniformly across the entire image.

*Statistical Analysis*

Statistical significance between age-matched wild-type and homozygous male *Obscn-ΔIg58/59* groups was determined by two-tailed Student's t-test in all experiments, excluding those depicted in Fig. 1D. A Fischer's exact test was used in Fig. 1D to compare Z-disk streaming. Error bars represent average values ± standard error of the mean (SEM). Sample sizes, cell, and animal numbers, along with the statistical tests and p values for each experiment are noted in the corresponding figure legends. Graphpad Prism (San Diego, CA) was used to calculate statistical parameters; *$p<0.05$, **$p<0.01$, ***$p<0.001$, and ****$p<0.0001$.

*Study Approval*

Animal care and procedures were conducted under protocols approved by the Institutional Animal Care and Use Committee at the University of Maryland, School of Medicine (UMSOM) and in accordance with the NIH guidelines (Guide for the Care and Use of Laboratory Animals).

*Data Availability*

Original images and blots are provided in the "Original Images & Blots" file and raw data values are supplied in the "Supporting Data Values" file.

**Sources of Funding**

This work was supported by the National Institutes of Health (Training Program in Muscle Biology, T32 AR007592 to A.G. and A.B., K99-R00 HL156005 to H.J., R01 HL142290 to C.W.W., and R01 AR077106 to A.K.K.), the UMB Institute for Clinical & Translational Research (ICTR-443 to A.K.K.), the Claude D. Pepper Older Americans Independence Center at the University of Maryland School of Medicine [P30 AG028747 to M.G.], and the BHF Intermediate Basic Science Research Fellowship [FS/IBSRF/24/25202 to LB].

## References


1. Goette A, Kalman JM, Aguinaga L, Akar J, Cabrera JA, Chen SA, et al. EHRA/HRS/APHRS/SOLAECE expert consensus on atrial cardiomyopathies: definition, characterization, and clinical implication. *Europace.* 2016;18(10):1455-90.
2. Lippi G, Sanchis-Gomar F, and Cervellin G. Global epidemiology of atrial fibrillation: An increasing epidemic and public health challenge. *Int J Stroke.* 2021;16(2):217-21.
3. Baman JR, Cox JL, McCarthy PM, Kim D, Patel RB, Passman RS, et al. Atrial fibrillation and atrial cardiomyopathies. *J Cardiovasc Electrophysiol.* 2021;32(10):2845-53.
4. Nishida K, Michael G, Dobrev D, and Nattel S. Animal models for atrial fibrillation: clinical insights and scientific opportunities. *Europace.* 2010;12(2):160-72.
5. Wijffels MC, Kirchhof CJ, Dorland R, and Allessie MA. Atrial fibrillation begets atrial fibrillation. A study in awake chronically instrumented goats. *Circulation.* 1995;92(7):1954-68.
6. D'Alessandro E, Winters J, van Nieuwenhoven FA, Schotten U, and Verheule S. The Complex Relation between Atrial Cardiomyopathy and Thrombogenesis. *Cells.* 2022;11(19).
7. Schuttler D, Bapat A, Kaab S, Lee K, Tomsits P, Clauss S, et al. Animal Models of Atrial Fibrillation. *Circ Res.* 2020;127(1):91-110.
8. Kontrogianni-Konstantopoulos A, Ackermann MA, Bowman AL, Yap SV, and Bloch RJ. Muscle giants: molecular scaffolds in sarcomerogenesis. *Physiol Rev.* 2009;89(4):1217-67.
9. Wang L, Geist J, Grogan A, Hu LR, and Kontrogianni-Konstantopoulos A. Thick Filament Protein Network, Functions, and Disease Association. *Compr Physiol.* 2018;8(2):631-709.
10. Grogan A, and Kontrogianni-Konstantopoulos A. Unraveling obscurins in heart disease. *Pflugers Arch.* 2019;471(5):735-43.
11. Chen P, Xiao Y, Wang Y, Zheng Z, Chen L, Yang X, et al. Intracellular calcium current disorder and disease phenotype in OBSCN mutant iPSC-based cardiomyocytes in arrhythmogenic right ventricular cardiomyopathy. *Theranostics.* 2020;10(24):11215-29.
12. Herrera-Rivero M, Gandhi S, Witten A, Ghalawinji A, Schotten U, and Stoll M. Cardiac chamber-specific genetic alterations suggest candidate genes and pathways implicating the left ventricle in the pathogenesis of atrial fibrillation. *Genomics.* 2022;114(2):110320.
13. Hu LR, Ackermann MA, Hecker PA, Prosser BL, King B, O'Connell KA, et al. Deregulated Ca(2+) cycling underlies the development of arrhythmia and heart disease due to mutant obscurin. *Sci Adv.* 2017;3(6):e1603081.
14. Young P, Ehler E, and Gautel M. Obscurin, a giant sarcomeric Rho guanine nucleotide exchange factor protein involved in sarcomere assembly. *J Cell Biol.* 2001;154(1):123-36.
15. Bang ML, Centner T, Fornoff F, Geach AJ, Gotthardt M, McNabb M, et al. The complete gene sequence of titin, expression of an unusual approximately 700-kDa titin isoform, and its interaction with obscurin identify a novel Z-line to I-band linking system. *Circ Res.* 2001;89(11):1065-72.
16. Grogan A, Coleman A, Joca H, Granzier H, Russel MW, Ward CW, et al. Deletion of obscurin immunoglobulin domains Ig58/59 leads to age-dependent cardiac remodeling and arrhythmia. *Basic Res Cardiol.* 2020;115(6):60.
17. Grogan A, Huang W, Brong A, Kane MA, and Kontrogianni-Konstantopoulos A. Alterations in cytoskeletal and Ca(2+) cycling regulators in atria lacking the obscurin Ig58/59 module. *Front Cardiovasc Med.* 2023;10:1085840.

18. Wadmore K, Azad AJ, and Gehmlich K. The Role of Z-disc Proteins in Myopathy and Cardiomyopathy. *Int J Mol Sci.* 2021;22(6).
19. Greiser M, and Schotten U. Dynamic remodeling of intracellular Ca(2)(+) signaling during atrial fibrillation. *J Mol Cell Cardiol.* 2013;58:134-42.
20. Hoang-Trong TM, Ullah A, and Jafri MS. Calcium Sparks in the Heart: Dynamics and Regulation. *Res Rep Biol.* 2015;6:203-14.
21. Cheng H, Lederer WJ, and Cannell MB. Calcium sparks: elementary events underlying excitation-contraction coupling in heart muscle. *Science.* 1993;262(5134):740-4.
22. Connell P, Word TA, and Wehrens XHT. Targeting pathological leak of ryanodine receptors: preclinical progress and the potential impact on treatments for cardiac arrhythmias and heart failure. *Expert Opin Ther Targets.* 2020;24(1):25-36.
23. Dridi H, Kushnir A, Zalk R, Yuan Q, Melville Z, and Marks AR. Intracellular calcium leak in heart failure and atrial fibrillation: a unifying mechanism and therapeutic target. *Nat Rev Cardiol.* 2020;17(11):732-47.
24. Greiser M, Kerfant BG, Williams GS, Voigt N, Harks E, Dibb KM, et al. Tachycardia-induced silencing of subcellular Ca2+ signaling in atrial myocytes. *J Clin Invest.* 2014;124(11):4759-72.
25. Kaplan AD, Boyman L, Ward CW, Lederer WJ, and Greiser M. Ryanodine receptor stabilization therapy suppresses Ca(2+)- based arrhythmias in a novel model of metabolic HFpEF. *J Mol Cell Cardiol.* 2024;195:68-72.
26. Furukawa T, Ono Y, Tsuchiya H, Katayama Y, Bang ML, Labeit D, et al. Specific interaction of the potassium channel beta-subunit minK with the sarcomeric protein T-cap suggests a T-tubule-myofibril linking system. *J Mol Biol.* 2001;313(4):775-84.
27. Ibrahim M, Siedlecka U, Buyandelger B, Harada M, Rao C, Moshkov A, et al. A critical role for Telethonin in regulating t-tubule structure and function in the mammalian heart. *Hum Mol Genet.* 2013;22(2):372-83.
28. Candasamy AJ, Haworth RS, Cuello F, Ibrahim M, Aravamudhan S, Kruger M, et al. Phosphoregulation of the titin-cap protein telethonin in cardiac myocytes. *J Biol Chem.* 2014;289(3):1282-93.
29. Gregorio CC, Trombitas K, Centner T, Kolmerer B, Stier G, Kunke K, et al. The NH2 terminus of titin spans the Z-disc: its interaction with a novel 19-kD ligand (T-cap) is required for sarcomeric integrity. *J Cell Biol.* 1998;143(4):1013-27.
30. Knoll R, Linke WA, Zou P, Miocic S, Kostin S, Buyandelger B, et al. Telethonin deficiency is associated with maladaptation to biomechanical stress in the mammalian heart. *Circ Res.* 2011;109(7):758-69.
31. Lewis HR, Eminaga S, Gautel M, and Avkiran M. Phosphorylation at Serines 157 and 161 Is Necessary for Preserving Cardiac Expression Level and Functions of Sarcomeric Z-Disc Protein Telethonin. *Front Physiol.* 2021;12:732020.
32. Wirianto M, Yang J, Kim E, Gao S, Paudel KR, Choi JM, et al. The GSK-3beta-FBXL21 Axis Contributes to Circadian TCAP Degradation and Skeletal Muscle Function. *Cell Rep.* 2020;32(11):108140.
33. Kinoshita E, Kinoshita-Kikuta E, and Koike T. History of Phos-tag technology for phosphoproteomics. *J Proteomics.* 2022;252:104432.
34. Gross P, Johnson J, Romero CM, Eaton DM, Poulet C, Sanchez-Alonso J, et al. Interaction of the Joining Region in Junctophilin-2 With the L-Type Ca(2+) Channel Is Pivotal for

765 Cardiac Dyad Assembly and Intracellular Ca(2+) Dynamics. *Circ Res.* 2021;128(1):92-
766 114.
767 35. Poulet C, Sanchez-Alonso J, Swiatlowska P, Mouy F, Lucarelli C, Alvarez-Laviada A, et
768 al. Junctophilin-2 tethers T-tubules and recruits functional L-type calcium channels to lipid
769 rafts in adult cardiomyocytes. *Cardiovasc Res.* 2021;117(1):149-61.
770 36. Weninger G, Pochechueva T, El Chami D, Luo X, Kohl T, Brandenburg S, et al. Calpain
771 cleavage of Junctophilin-2 generates a spectrum of calcium-dependent cleavage products
772 and DNA-rich NT(1)-fragment domains in cardiomyocytes. *Sci Rep.* 2022;12(1):10387.
773 37. Guo A, Wang Y, Chen B, Wang Y, Yuan J, Zhang L, et al. E-C coupling structural protein
774 junctophilin-2 encodes a stress-adaptive transcription regulator. *Science.* 2018;362(6421).
775 38. Hoshijima M. Mechanical stress-strain sensors embedded in cardiac cytoskeleton: Z disk,
776 titin, and associated structures. *Am J Physiol Heart Circ Physiol.* 2006;290(4):H1313-25.
777 39. Purevjav E, and Towbin JA. The Z-disk final common pathway in cardiomyopathies. 2021.
778 40. Berchtold MW, Munk M, Kulej K, Porth I, Lorentzen L, Panina S, et al. The heart
779 arrhythmia-linked D130G calmodulin mutation causes premature inhibitory
780 autophosphorylation of CaMKII. *Biochim Biophys Acta Mol Cell Res.*
781 2021;1868(12):119119.
782 41. Song LS, Sobie EA, McCulle S, Lederer WJ, Balke CW, and Cheng H. Orphaned
783 ryanodine receptors in the failing heart. *Proc Natl Acad Sci U S A.* 2006;103(11):4305-10.
784 42. Lenaerts I, Bito V, Heinzel FR, Driesen RB, Holemans P, D'Hooge J, et al. Ultrastructural
785 and functional remodeling of the coupling between Ca2+ influx and sarcoplasmic
786 reticulum Ca2+ release in right atrial myocytes from experimental persistent atrial
787 fibrillation. *Circ Res.* 2009;105(9):876-85.
788 43. Brandenburg S, Kohl T, Williams GS, Gusev K, Wagner E, Rog-Zielinska EA, et al. Axial
789 tubule junctions control rapid calcium signaling in atria. *J Clin Invest.* 2016;126(10):3999-
790 4015.
791 44. Denham NC, Pearman CM, Caldwell JL, Madders GWP, Eisner DA, Trafford AW, et al.
792 Calcium in the Pathophysiology of Atrial Fibrillation and Heart Failure. *Front Physiol.*
793 2018;9:1380.
794 45. Voigt N, Heijman J, Wang Q, Chiang DY, Li N, Karck M, et al. Cellular and molecular
795 mechanisms of atrial arrhythmogenesis in patients with paroxysmal atrial fibrillation.
796 *Circulation.* 2014;129(2):145-56.
797 46. Voigt N, Li N, Wang Q, Wang W, Trafford AW, Abu-Taha I, et al. Enhanced sarcoplasmic
798 reticulum Ca2+ leak and increased Na+-Ca2+ exchanger function underlie delayed
799 afterdepolarizations in patients with chronic atrial fibrillation. *Circulation.*
800 2012;125(17):2059-70.
801 47. Camors E, and Valdivia HH. CaMKII regulation of cardiac ryanodine receptors and
802 inositol triphosphate receptors. *Front Pharmacol.* 2014;5:101.
803 48. Yuchi Z, Lau K, and Van Petegem F. Disease mutations in the ryanodine receptor central
804 region: crystal structures of a phosphorylation hot spot domain. *Structure.*
805 2012;20(7):1201-11.
806 49. Bootman MD, Smyrnias I, Thul R, Coombes S, and Roderick HL. Atrial cardiomyocyte
807 calcium signalling. *Biochim Biophys Acta.* 2011;1813(5):922-34.
808 50. Walden AP, Dibb KM, and Trafford AW. Differences in intracellular calcium homeostasis
809 between atrial and ventricular myocytes. *J Mol Cell Cardiol.* 2009;46(4):463-73.

51. Ko D, Rahman F, Schnabel RB, Yin X, Benjamin EJ, and Christophersen IE. Atrial fibrillation in women: epidemiology, pathophysiology, presentation, and prognosis. *Nat Rev Cardiol.* 2016;13(6):321-32.
52. Odening KE, Deiß S, Dilling-Boer D, Didenko M, Eriksson U, Nedios S, et al. Mechanisms of sex differences in atrial fibrillation: role of hormones and differences in electrophysiology, structure, function, and remodelling. *Europace.* 2019;21(3):366-76.
53. Kasi VS, Xiao HD, Shang LL, Iravanian S, Langberg J, Witham EA, et al. Cardiac-restricted angiotensin-converting enzyme overexpression causes conduction defects and connexin dysregulation. *Am J Physiol Heart Circ Physiol.* 2007;293(1):H182-92.
54. Saba S, Janczewski AM, Baker LC, Shusterman V, Gursoy EC, Feldman AM, et al. Atrial contractile dysfunction, fibrosis, and arrhythmias in a mouse model of cardiomyopathy secondary to cardiac-specific overexpression of tumor necrosis factor-{alpha}. *Am J Physiol Heart Circ Physiol.* 2005;289(4):H1456-67.
55. Deerinck T.J., Bushong E., Thor A, and Ellisman M.H. NCMIR methods for 3D EM: a new protocol for preparation of biological specimens for serial block face scanning electron microscopy. *Nat Center Microsc Imag Res.* 2010.
56. Shioya T. A simple technique for isolating healthy heart cells from mouse models. *J Physiol Sci.* 2007;57(6):327-35.
57. Garber L, Joca HC, Coleman AK, Boyman L, Lederer WJ, and Greiser M. Camera-based Measurements of Intracellular [Na+] in Murine Atrial Myocytes. *J Vis Exp.* 2022(183).
58. Joca HC. CaTanalysis. https://github.com/humberojoca/CaTanalysis.git.
59. Picht E, Zima AV, Blatter LA, and Bers DM. SparkMaster: automated calcium spark analysis with ImageJ. *Am J Physiol Cell Physiol.* 2007;293(3):C1073-81.
60. Hollingworth S, Peet J, Chandler WK, and Baylor SM. Calcium sparks in intact skeletal muscle fibers of the frog. *J Gen Physiol.* 2001;118(6):653-78.
61. Greiser M, Karbowski M, Kaplan AD, Coleman AK, Verhoeven N, Mannella CA, et al. Calcium and bicarbonate signaling pathways have pivotal, resonating roles in matching ATP production to demand. *Elife.* 2023;12.
62. Schindelin J, Arganda-Carreras I, Frise E, Kaynig V, Longair M, Pietzsch T, et al. Fiji: an open-source platform for biological-image analysis. *Nat Methods.* 2012;9(7):676-82.
63. Yue X, Zhang R, Kim B, Ma A, Philipson KD, and Goldhaber JI. Heterogeneity of transverse-axial tubule system in mouse atria: Remodeling in atrial-specific Na(+)-Ca(2+) exchanger knockout mice. *J Mol Cell Cardiol.* 2017;108:50-60.
64. Boyman L. cardiomyocyte-transverse-axial-tubules-structure-analysis. https://github.com/lboyman1/cardiomyocyte-transverse-axial-tubules-structure-analysis.git.

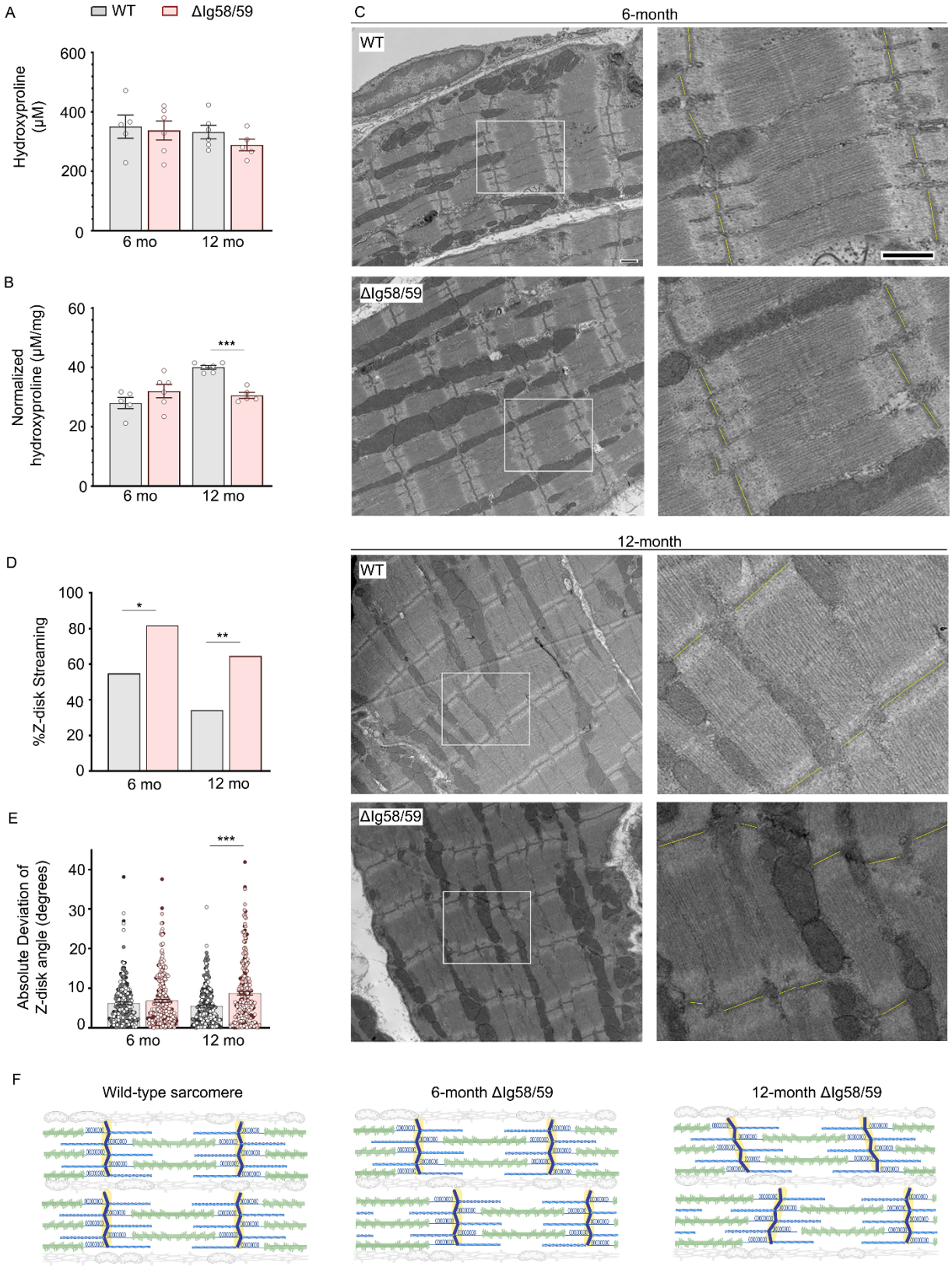
A
WT
ΔIg58/59
Hydroxyproline (μM)
600
400
200
0
6 mo
12 mo
B
Normalized hydroxyproline (μM/mg)
60
40
20
0
***
6 mo
12 mo
C
6-month
WT
ΔIg58/59
12-month
WT
ΔIg58/59
D
%Z-disk Streaming
100
80
60
40
20
0
*
**
6 mo
12 mo
E
Absolute Deviation of Z-disk angle (degrees)
40
30
20
10
0
***
6 mo
12 mo
F
Wild-type sarcomere
6-month ΔIg58/59
12-month ΔIg58/59

846

**Figure 1. Ultrastructural analysis reveals Z-disk abnormalities in *Obscn-ΔIg58/59* atria. (A-B)** Quantification of absolute hydroxyproline content (A) in atrial tissues did not reveal differences in fibrotic deposition between genotypes at 6- or 12-months. In contrast, when normalized to atrial tissue mass (B), hydroxyproline content was significantly reduced in *Obscn-ΔIg58/59* atria at 12-months compared to age-matched wild-type, indicating that the atrial enlargement observed in *Obscn-ΔIg58/59* mice at this timepoint is not associated with increased fibrosis; t-test, ***$p<0.001$; n=5-6 animals per group; data points represent the average of six technical replicates per animal. **(C)** Representative electron micrographs of longitudinally sectioned atria depicted Z-disk streaming in *Obscn-ΔIg58/59* hearts at 6- and 12-months, along with increased variability in Z-disk orientation at 12-months; scale bar: 500 nm. Z-disks are highlighted in yellow in the images on the right, which are zoomed-in areas of the electron micrographs on the left, denoted by white rectangles. **(D)** The percent of images that contained Z-disk streaming was significantly increased in 6- and 12-month *Obscn-ΔIg58/59* atria compared to controls; Fisher's exact test, *$p<0.05$, **$p<0.01$; n=3 animals per group, 10±3 images per animal (6-months), 15±3 images per animal (12-months). **(E)** *Obscn-ΔIg58/59* atrial sarcomeres displayed significantly increased variability in the orientation of the Z-disk at 12-months as quantified by the absolute deviation of the Z-disk angle within each image; t-test, ***$p<0.001$; n=3 animals per group, 2 images per animal; data points represent individual sarcomeres and are color-coded by biological replicate. **(F)** Schematic illustrating the progressive changes in Z-disk architecture in *Obscn-ΔIg58/59*. While wild-type sarcomeres are properly aligned, Z-disks in *Obscn-ΔIg58/59* atria are out-of-register (i.e. Z-disk streaming) by 6-months and nonparallel by 12-months. Figure generated with Biorender.com (License *MB27PC5ZUC).*

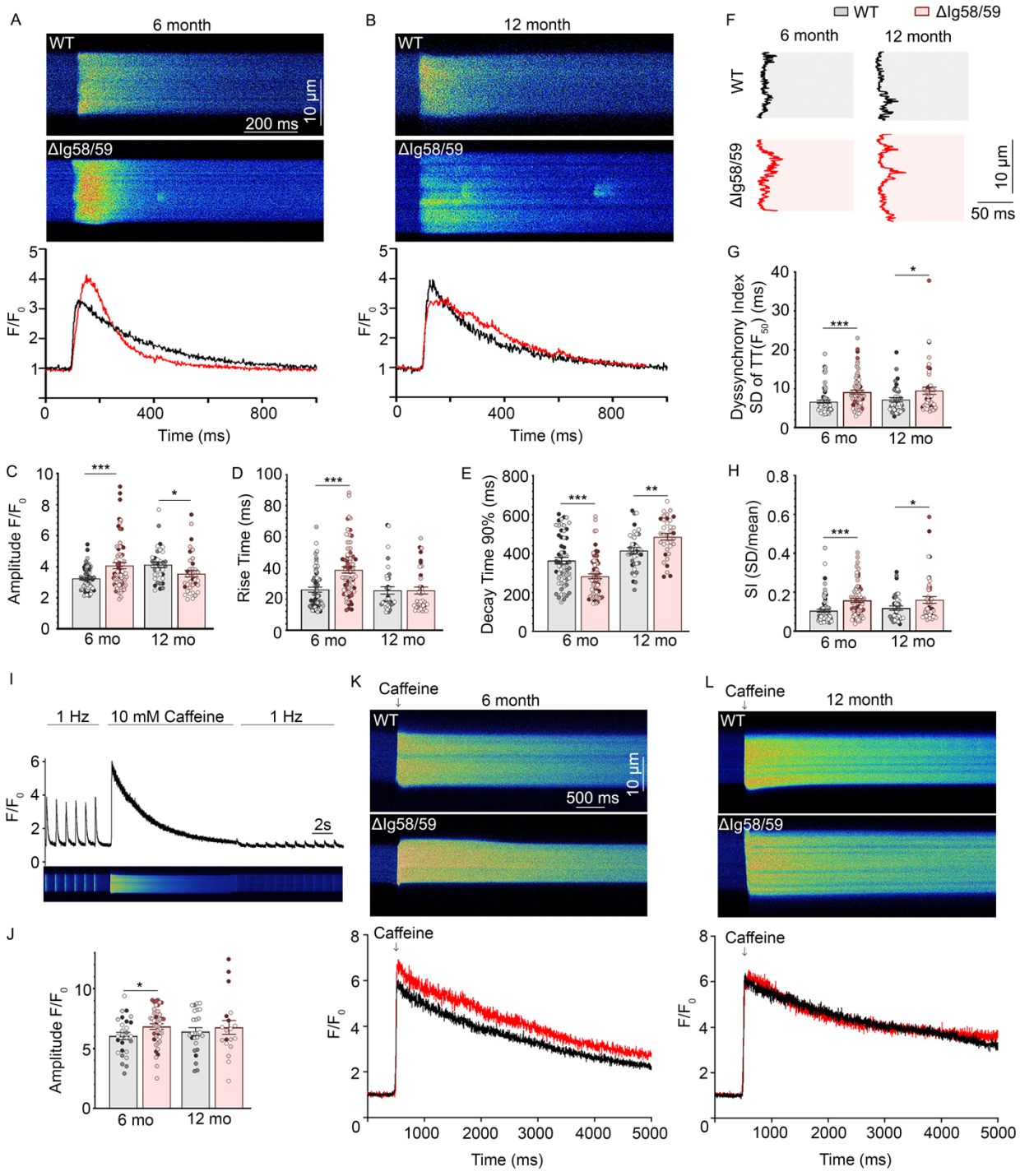


**Figure 2. Atrial cardiomyocytes from sedentary *Obscn-ΔIg58/59* mice exhibit age-specific changes in $Ca^{2+}$ cycling and SR $Ca^{2+}$ content. (A-E)** Representative confocal line scan images

and corresponding $Ca^{2+}$ transients (A-B) depicted significantly increased $Ca^{2+}$ transient amplitude (C) and rise time (D), and decreased $Ca^{2+}$ decay time (E) in atrial cardiomyocytes from 6-month-old *Obscn-ΔIg58/59* hearts compared to age-matched wild-type, whereas 12-month-old *Obscn-ΔIg58/59* cells displayed significantly decreased $Ca^{2+}$ transient amplitude (C) and prolonged $Ca^{2+}$ decay (E) compared to controls, with no change in rise time (D); t-test, *p<0.05, **p<0.01, ***p<0.001; n=5 animals per group (6-months), n=3 animals per group (12-months), 9-20 cells per heart (6-months), 7-17 cells per heart (12-months), data points represent individual cells and are color-coded by biological replicate. **(F)** Line profiles of the representative $Ca^{2+}$ transients depicted in (A-B) at half-maximal fluorescence amplitude and corresponding quantifications of the standard deviation (SD) of the time to half-maximal fluorescence ($TTF_{50}$; **G**) and the coefficient of variation, SI **(H)**, revealed dyssynchronous $Ca^{2+}$ release in *Obscn-ΔIg58/59* atria at 6- and 12-months; t-test, *p<0.05, ***p<0.001; n=5 animals per group (6-months), n=3-4 animals per group (12-months), 6-24 cells per heart (6-months), 2-17 cells per heart (12-months); data points represent individual cells and are color-coded by biological replicate. **(I-L)** SR $Ca^{2+}$ load was measured in quiescent atrial cardiomyocytes via rapid application of 10 mmol/L caffeine preceded by steady-state 1 Hz electrical pacing. Field stimulation was subsequently restarted to ensure that all releasable $Ca^{2+}$ had been depleted (I). Representative transverse confocal line scan images and caffeine-induced $Ca^{2+}$ transients at 6-months (K) and 12-months (L) depicted significantly increased SR $Ca^{2+}$ content (J) in atrial cardiomyocytes isolated from 6-month-old *Obscn-ΔIg58/59* hearts, but not at 12-months, compared to age-matched controls; t-test, *p<0.05; n=4-5 animals per group (6-months), n=3-4 animals per group (12-months), 5-11 cells per heart (6-months), 2-11 cells per heart (12-months); data points represent individual cells and are color-coded by biological replicate.

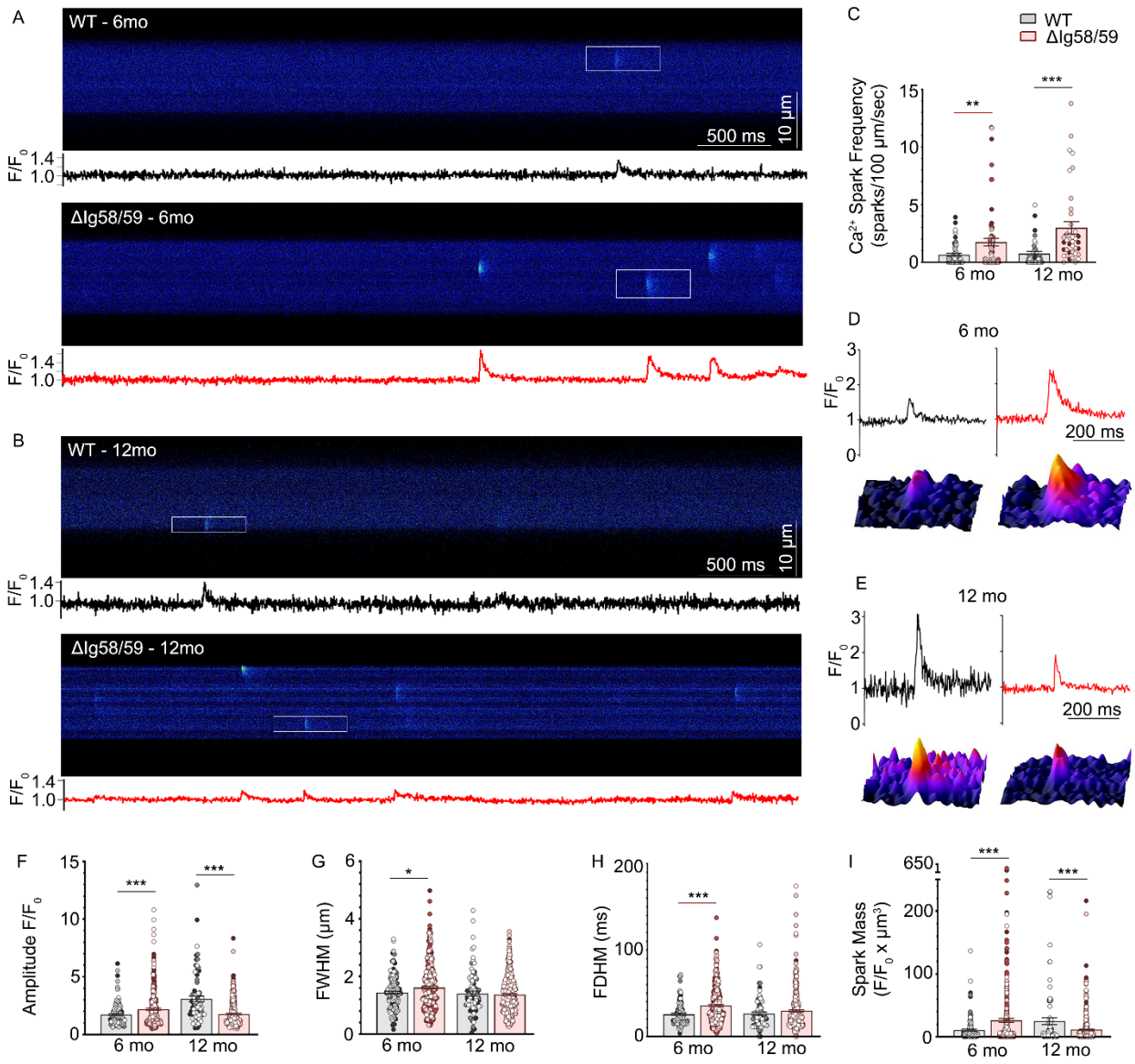


**Figure 3. Elevated $Ca^{2+}$ spark frequency in atrial cardiomyocytes from *Obscn-ΔIg58/59* mice.** **(A-B)** Representative confocal line scan traces and corresponding fluorescence intensity profiles of un-stimulated wild-type and *Obscn-ΔIg5859* atrial cells at 6-months (A) and 12-months (B). **(C)** Cells isolated from *Obscn-ΔIg5859* atria displayed a ~2.6 and ~4.0 fold increase in spark frequency compared to wild-type at 6- and 12-months, respectively; t-test, **p<0.01, ***p<0.001; data points represent individual cells and are color-coded by biological replicate. **(D-E)** Fluorescence intensity profiles and corresponding 3-Dimensional surface plots of representative

$Ca^{2+}$ sparks indicated by white rectangles in (A-B) from wild-type and *Obscn-ΔIg5859* atria at 6-months (D) and 12-months (E). **(F-I)** $Ca^{2+}$ spark analysis revealed significantly increased spark amplitude (F), FWHM (G), FDHM (H), and spark mass (I) in 6-month-old *Obscn-ΔIg5859* cells compared to wild-type, whereas 12 -month *Obscn-ΔIg5859* cells displayed significantly decreased spark amplitude (F) and spark mass (I) with no changes in FWHM (G) or FDHM (H); t-test, *p<0.05, ***p<0.001; n= 5 animals per group (6-months), n=3 animals per group (12-months), 9-20 cells per heart (6-months), 7-17 cells per heart (12-months); data points represent individual sparks and are color-coded by biological replicate.

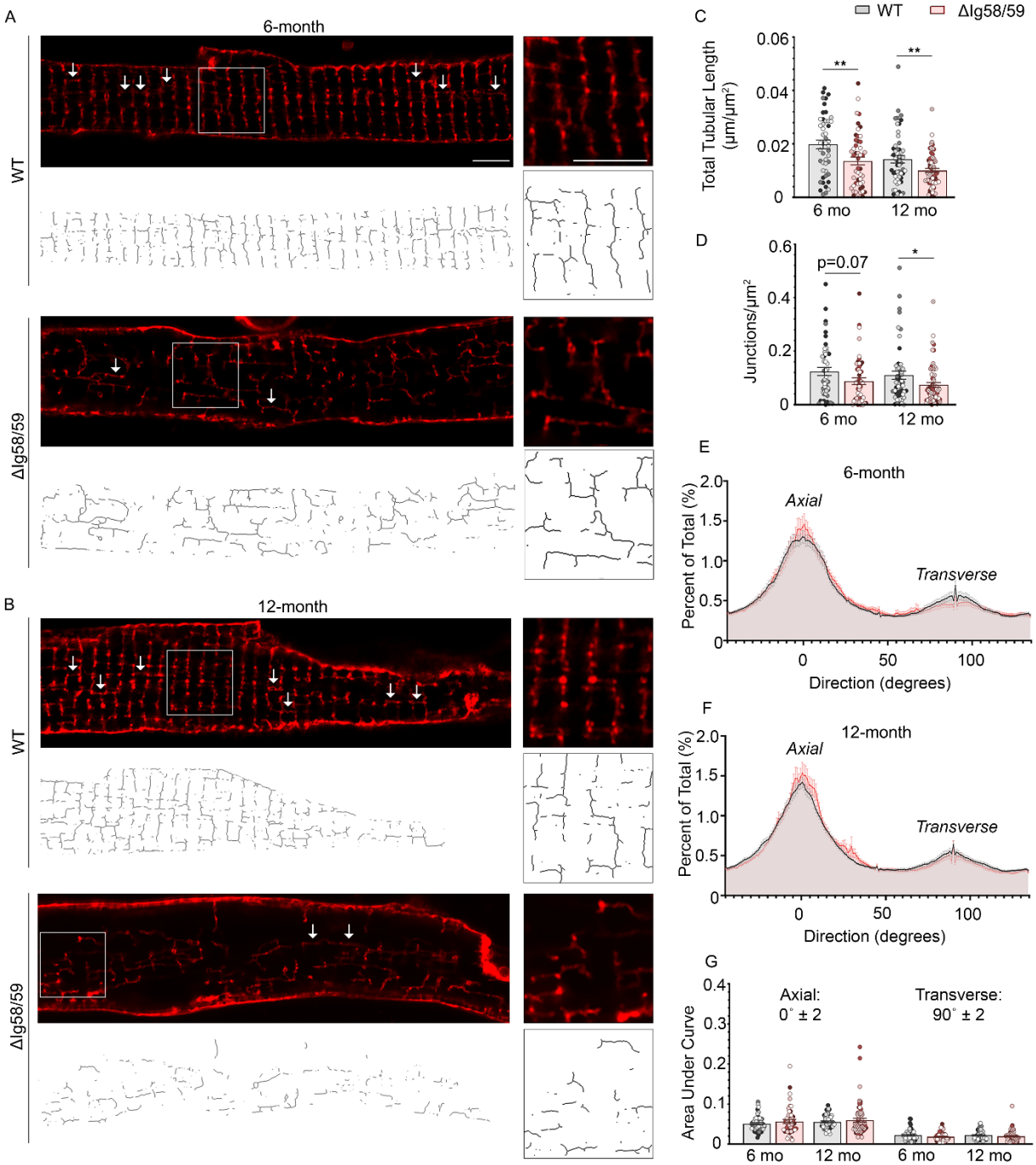


**Figure 4. The transverse-axial tubule network is disrupted in *Obscn-ΔIg58/59* atria. (A-B)** Representative super resolution images of wild-type and *Obscn-ΔIg5859* atrial cardiomyocytes stained with di-8-ANEPPS at 6-months (A) and 12-months (B); arrows highlight axial tubule structures; scale bar: 5 μm. **(C-D)** The total length of the tubular network (C) is decreased in *Obscn-ΔIg58/59* atria at both 6- and 12-months, while the number of tubular junctions (D) is

919 significantly diminished by 12-months; t-test, *p<0.05, **p<0.01. **(E-G)** Histograms depicting the
920 proportion of tubules at each orientation at 6- (E) and 12- (F) months and corresponding
921 quantifications (G) did not indicate any differences in the distribution of axial and transverse
922 tubules in *Obscn-ΔIg5859* cells compared to wild-type; t-test, 0˚: p=0.34 (6-months), p=0.43 (12-
923 months), 90˚: p=0.13 (6-months), p=0.27 (12-months); area under the curve was calculated within
924 a range of ± 2˚ from 0˚ (axial) or 90˚ (transverse); n=4 animals per group (6-months), n=4-6
925 animals per group (12-months), 9-14 cells per heart (6-months), 6-19 cells per heart (12-months);
926 data points represent individual cells and are color-coded by biological replicate.

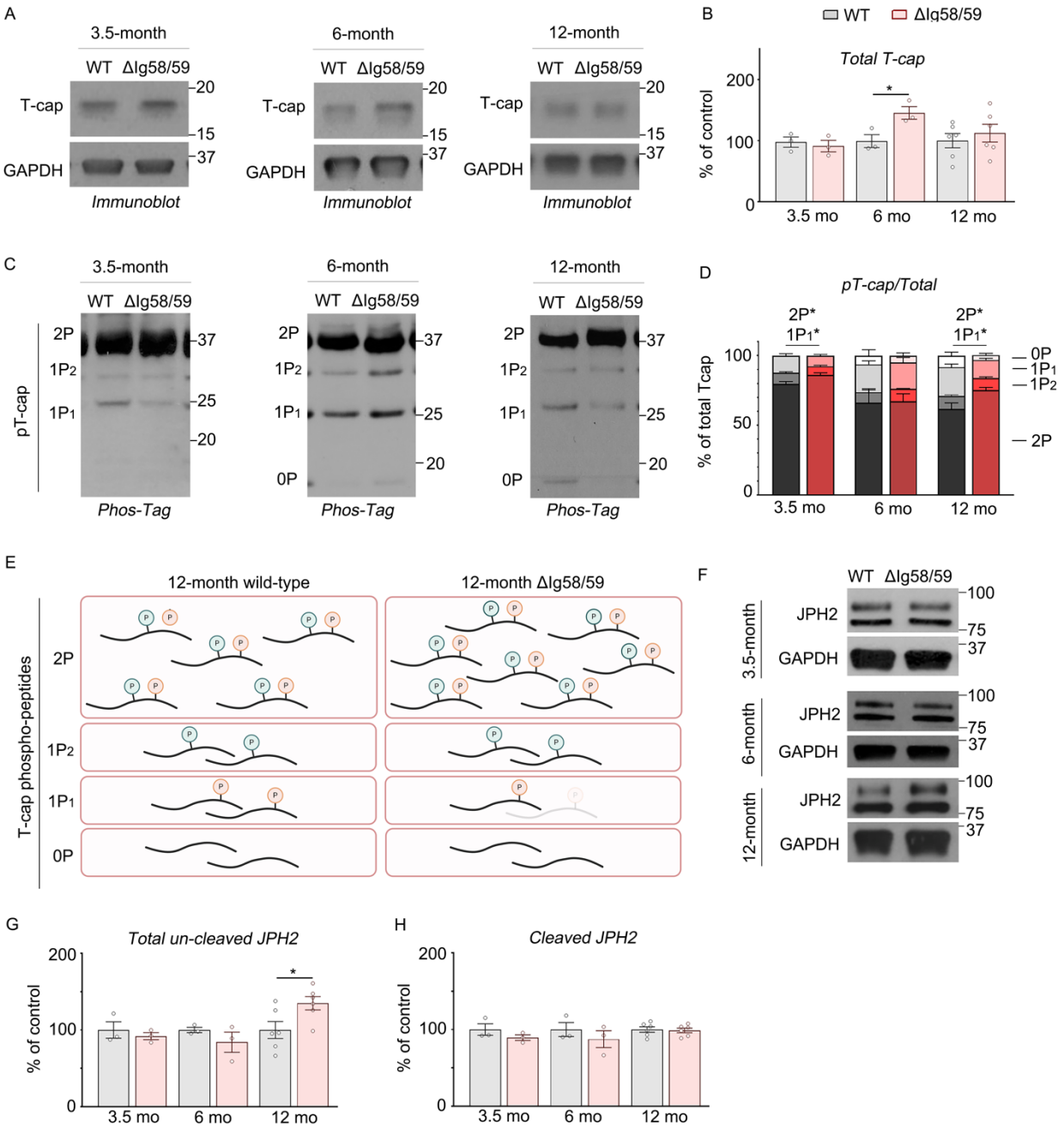


**Figure 5. The expression and phosphorylation of T-cap is altered in *Obscn-ΔIg58/59* atria.** **(A-B)** Representative immunoblots (A) and relative quantifications (B) revealed significantly increased T-cap expression in *Obscn-ΔIg5859* atria compared to wild-type at 6-months, but not at 3.5- or 12-months. **(C-D)** Representative Phos-Tag™ acrylamide immunoblots (C) and relative quantifications (D) did not indicate significant differences in normalized pT-cap at 6-months, but

revealed increased levels of bi-phosphorylated T-cap (2P) and a corresponding decrease in the lower molecular weight mono-phosphorylated ($1P_1$) T-cap species with no statistically significant differences in the higher molecular weight ($1P_2$) or non-phosphorylated (0P) T-cap species in *Obscn-ΔIg5859* atria compared to wild-type at both 3.5- and 12-months. Non-phosphorylated (0P) T-cap species were not reliably detected at 3.5-months and therefore were not quantified; t-test, *$p<0.05$; 5a: n=3 animals per genotype for the 3.5- and 6-month timepoints and n=6 animals per genotype for the 12-month timepoint; 5b: n=6 animals per genotype for the 3.5-month timepoint, n=3 animals per genotype for the 6-month timepoint, and n=5 animals per genotype for the 12-month timepoint; data points represent the average of at least three technical replicates per animal; quantifications of phosphorylated T-cap were normalized to the summed intensity of all species for a given sample. **(E)** Schematic depicting the decrease in $1P_1$ T-cap species and corresponding increase in 2P T-cap observed in *Obscn-ΔIg5859* atria at 12-months. Figure generated with Biorender.com (License *OT27PC68YH*). **(F-H)** Representative immunoblots (F) and relative quantifications (G-H) revealed significantly increased total un-cleaved junctophilin-2 (JPH2), but not cleaved JPH2 NT1, in *Obscn-ΔIg5859* atria compared to wild-type at 12-months; t-test, *$p<0.05$; n=3 animals per group (3.5- and 6-months), n=6 animals per group (12-months); data points represent the average of at least three technical replicates per animal.

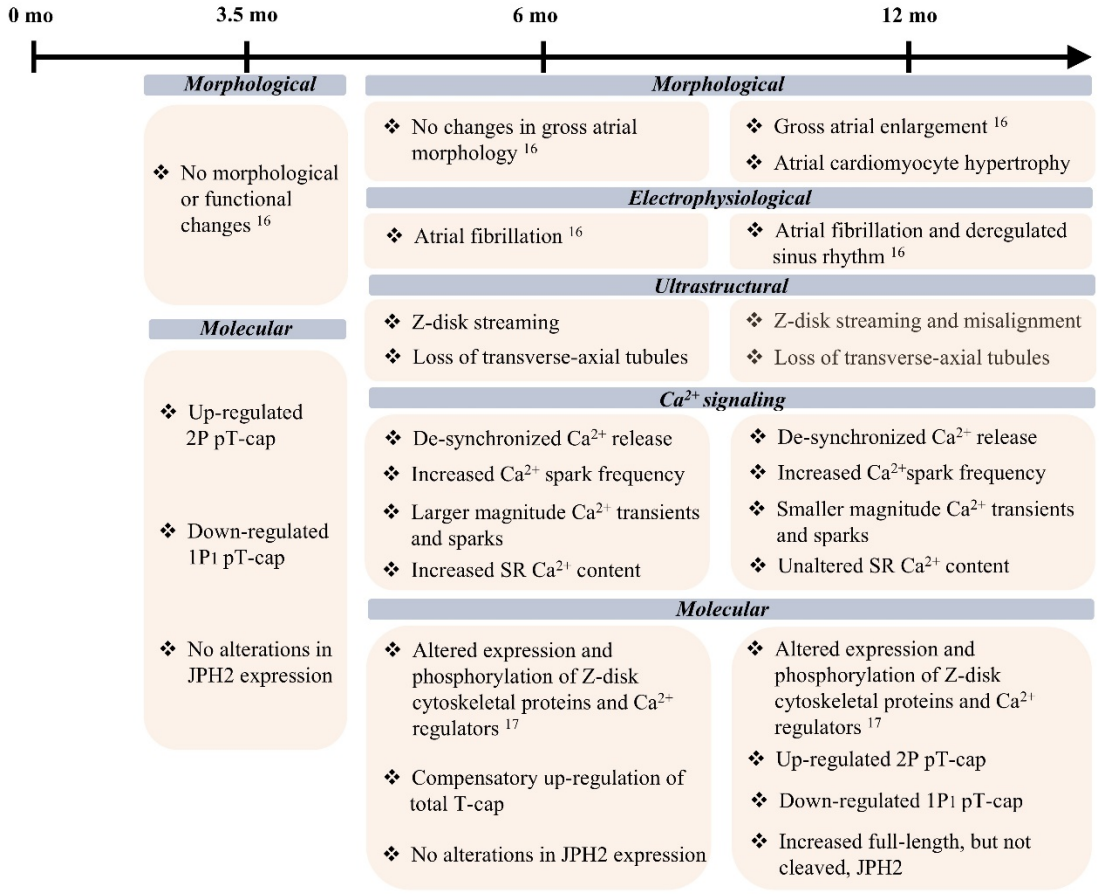


**Figure 6. The *Obscn-ΔIg58/59* atrial phenotype.** The phosphorylation profile of T-cap is dysregulated prior to the onset of arrhythmia and cardiac remodeling (16) in *Obscn-ΔIg58/59* atria at 3.5-months. Between the ages of 6- and 12-months, *Obscn-ΔIg58/59* mice undergo progressive structural remodeling and $Ca^{2+}$ dysregulation accompanied by changes in T-cap expression and phosphorylation as well as junctophilin-2 expression that align with the onset and progression of AF.

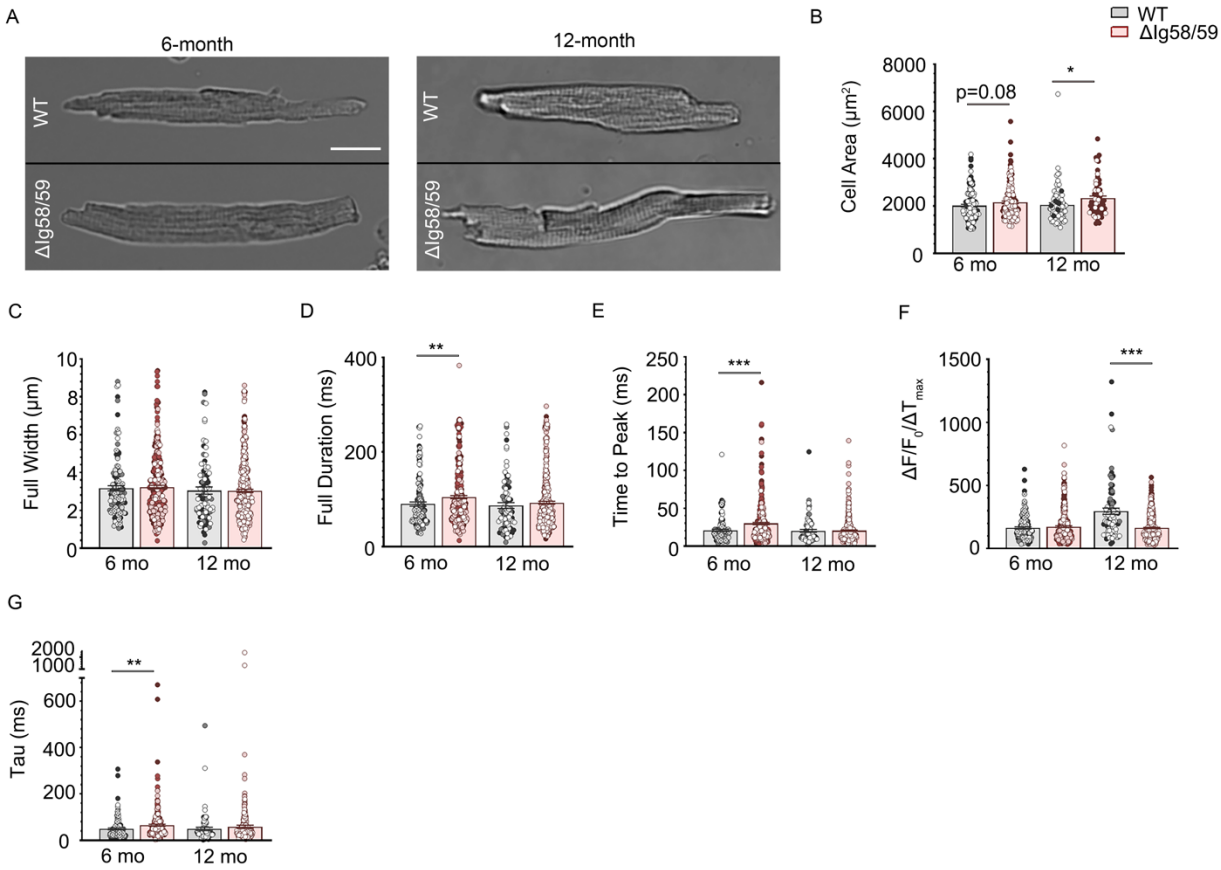


959

960 **SFigure 1. Evaluation of $Ca^{2+}$ spark morphology and $Ca^{2+}$ in *Obscn-ΔIg5859* atria at 6- and**
961 **12- months. (A-B)** Cardiomyocytes isolated from *Obscn-ΔIg58/59* atria were significantly
962 enlarged at 12-months of age compared to age-matched wild-type; scale bar: 20 μm; t-test,
963 *p<0.05; n=2 animals per group, 60-101 cells per heart (6-months), 7-83 cells per heart (12-
964 months); data points represent individual cells and are color-coded by biological replicate. **(C-G)**
965 Analysis of $Ca^{2+}$ spark morphology revealed no significant differences in full width (C), and age-
966 specific alterations in full duration (D), time to peak (E), the maximum steepness of spark upstroke
967 calculated as $\Delta F/F_0/\Delta T_{max}$ (F), and the exponential time constant of decay, Tau (G) in *Obscn-*
968 *ΔIg5859* atria at 6- and 12- months; t-test, **p<0.01***p<0.001, n= 5 animals per group (6-
969 months), n=3 animals per group (12-months); 9-20 cells per heart (6-months), 7-17 cells per heart
970 (12-months); data points represent individual sparks and are color-coded by biological replicate.

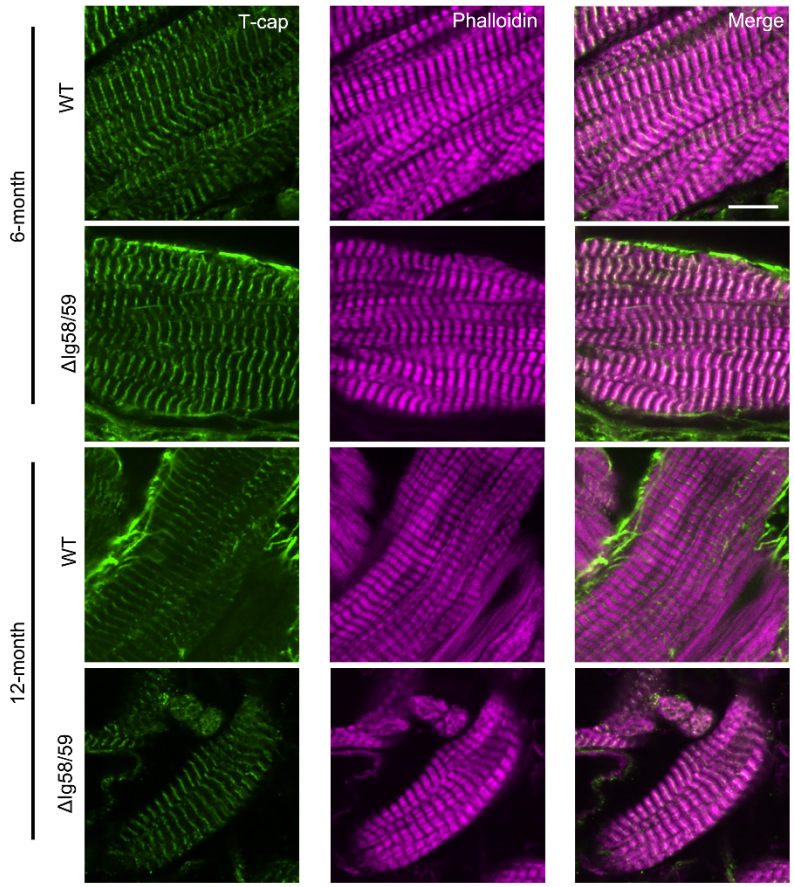


971

972 **SFigure 2. The localization of T-cap is unchanged in *Obscn-ΔIg58/59* atria.** Immunostained
973 cryosections of wild-type and *Obscn-ΔIg5859* atrial tissues indicated that T-cap is properly
974 localized to the Z-disk at both 6- and 12-months as determined by co-staining with the actin
975 marker, phalloidin; scale bar: 10 μm.

976

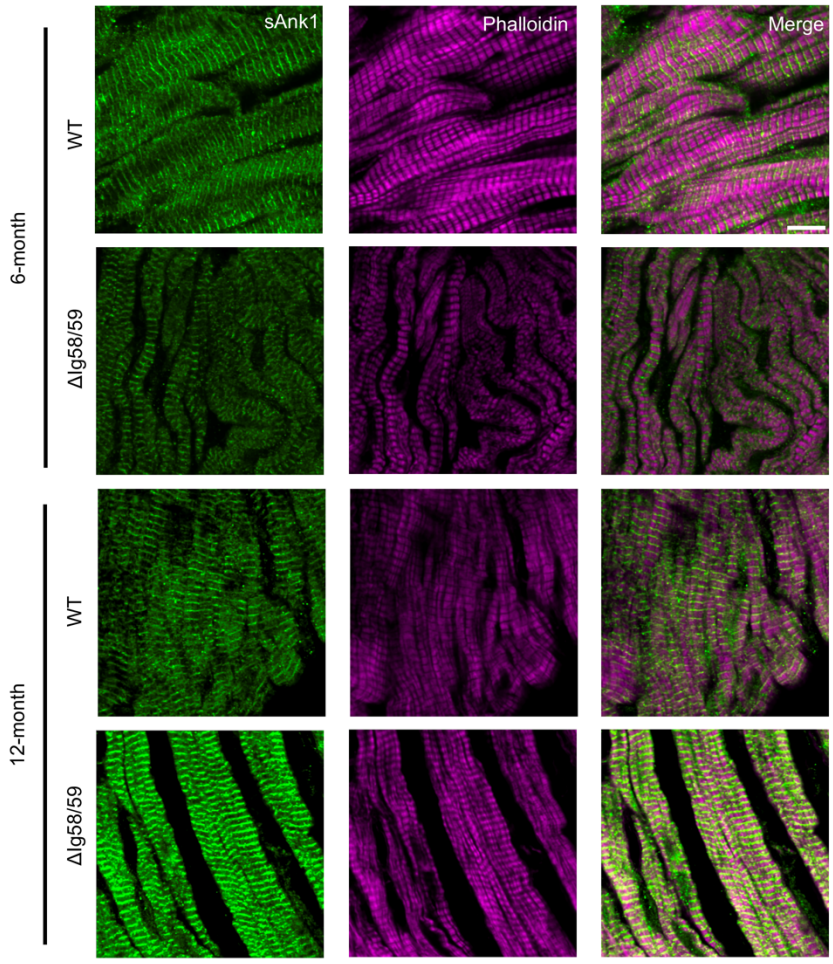


**SFigure 3. The localization of sAnk1 is unchanged in *Obscn-ΔIg58/59* atria.** Immunostained cryosections of wild-type and *Obscn-ΔIg5859* atrial tissues do not indicate alterations in sAnk1 localization at 6- or 12-months as determined by co-staining with the actin marker, phalloidin, suggesting the structure of the SR is unaffected in *Obscn-ΔIg5859* atria; scale bar: 10 μm.

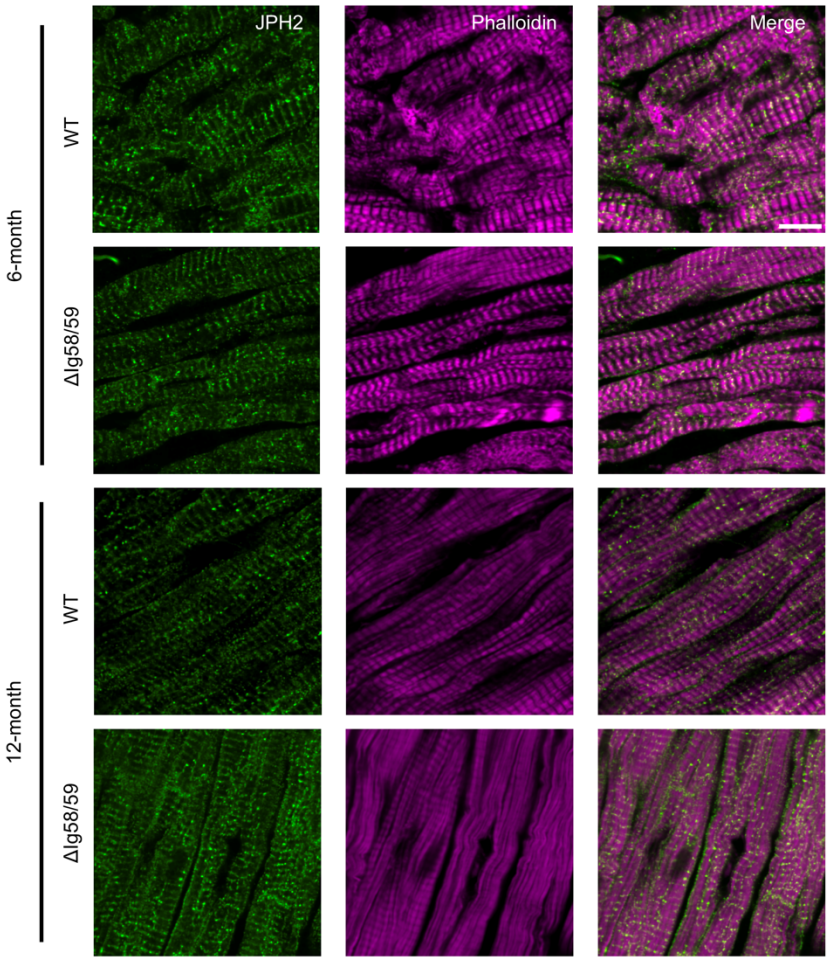


**SFigure 4. The localization of JPH2 is unchanged in *Obscn-ΔIg58/59* atria.** Immunostained cryosections of wild-type and *Obscn-ΔIg5859* atrial tissues do not indicate alterations in JPH2 localization at 6- or 12-months as determined by co-staining with the actin marker, phalloidin, suggesting that the junctional SR is unaffected in *Obscn-ΔIg5859* atria; scale bar: 10 µm.